Astronomy
&
Astrophysics

Stellar evolution with rotation

VIII. Models at $Z = 10^{-5}$ and CNO yields for early galactic evolution

G. Meynet and A. Maeder

Geneva Observatory, 1290 Sauverny, Switzerland
e-mail: Andre.Maeder@obs.unige.ch

Abstract. We calculate a grid of star models with and without the effects of axial rotation for stars in the mass range between 2 and 60 $M_\odot$ for the metallicity $Z = 10^{-5}$. Star models with initial masses superior or equal to 9 $M_\odot$ were computed up to the end of the carbon–burning phase. Star models with masses between 2 and 7 $M_\odot$ were evolved beyond the end of the He–burning phase through a few thermal pulses during the AGB phase. Compared to models at $Z = 0.02$, the low Z models show faster rotating cores and stronger internal Ω–gradients, which favour an important mixing of the chemical elements. The enhancement of N/C at the surface may reach 2 to 3 orders of magnitude for fast rotating stars. Surface enrichments may make the evolved stars less metal poor than they were initially. In very low Z models, primary nitrogen is produced during the He–burning phase by rotational diffusion of ^{12}C into the H–burning shell. A large fraction of the primary ^{14}N escapes further destruction and enters the envelope of AGB stars, being ejected during the TP–AGB phase and the formation of a planetary nebula. The intermediate mass stars of very low Z are the main producers of primary ^{14}N, but massive stars also contribute to this production; no significant primary nitrogen is made in models at metallicity $Z = 0.004$ or above. We calculate the chemical yields in He, C, N, O and heavy elements and discuss the chemical evolution of the CNO elements at very low Z. Remarkably, the C/O vs. O/H diagram is mainly sensitive to the interval of stellar masses, while the N/O vs. O/H diagram is mainly sensitive to the average rotation of the stars contributing to the element synthesis. The presently available observations in these diagrams seem to favour contributions either from stars down to about 2 $M_\odot$ with normal rotation velocities or from stars above 8 $M_\odot$ but with very fast rotation.

Key words. nuclear reactions, nucleosynthesis, abundances – stars: interiors – stars: evolution – stars: rotation – stars: early-types – stars: AGB and post-AGB

1. Introduction

Stellar rotation modifies all the outputs of stellar evolution for massive stars (Heger et al. 2000a; Heger & Langer 2000; Meynet & Maeder 2000). This is true at solar metallicity. At lower metallicities, like $Z = 0.004$ in the SMC, we noticed that the effects of rotation are expected to be larger (Maeder & Meynet 2001). In particular, for similar initial distributions of the rotational velocities, a larger fraction of the stars at lower Z reach break–up velocities. This is a result of the smaller losses of angular momentum by the stellar winds.

In addition, it may be that the initial distribution of the rotational velocities is not the same at lower Z. Indeed, it has been shown (Maeder et al. 1999) that the fraction of Be stars (i.e. stars close to break–up) is much higher in the SMC than in the Milky Way. However, we do not know whether this is just a consequence of the smaller mass loss, as said above, or whether the initial distribution of rotation velocities is also different as a result of processes of star formation at low Z. Whatever the exact origin of the higher fraction of stars close to break–up

at lower Z, this shows the need of studies of star models with rotation at low Z.

We consider here star models with metallicity $Z = 10^{-5}$, which is low enough to correspond to the most extreme metallicity observed in halo stars of the order of [Fe/H] $\simeq -3$ and which nevertheless avoid the particularities of $Z = 0$ models, which we may consider in a future paper. The main possible comparisons with the observations will concern the chemical evolution of the abundances of the CNO elements and of other heavy elements in halo stars and very low Z galaxies. This is why we put here a particular emphasis on the chemical yields in CNO at very low [Fe/H]. This is a topical point in relation with the problem of primary nitrogen (Edmunds & Pagel 1978; Barbuy 1983; Carbon et al. 1987; Thuan et al. 1995; Izotov & Thuan 1999; Henry et al. 2000). Also, the recent debate around the behavior of the [O/Fe] ratio at very low Z (cf. Israelian et al. 2001; Melendez et al. 2001) shows the need of a better understanding of the CNO yields at very low metallicities.

In Sect. 2, we discuss the model physics. In Sect. 3, we examine the internal rotation and the surface velocities in Sect. 4. The models with zero rotation are briefly mentioned in Sect. 5. The HR diagram and lifetimes are discussed in Sect. 6.

Send offprint requests to: G. Meynet,
e-mail: Georges.Meynet@obs.unige.ch
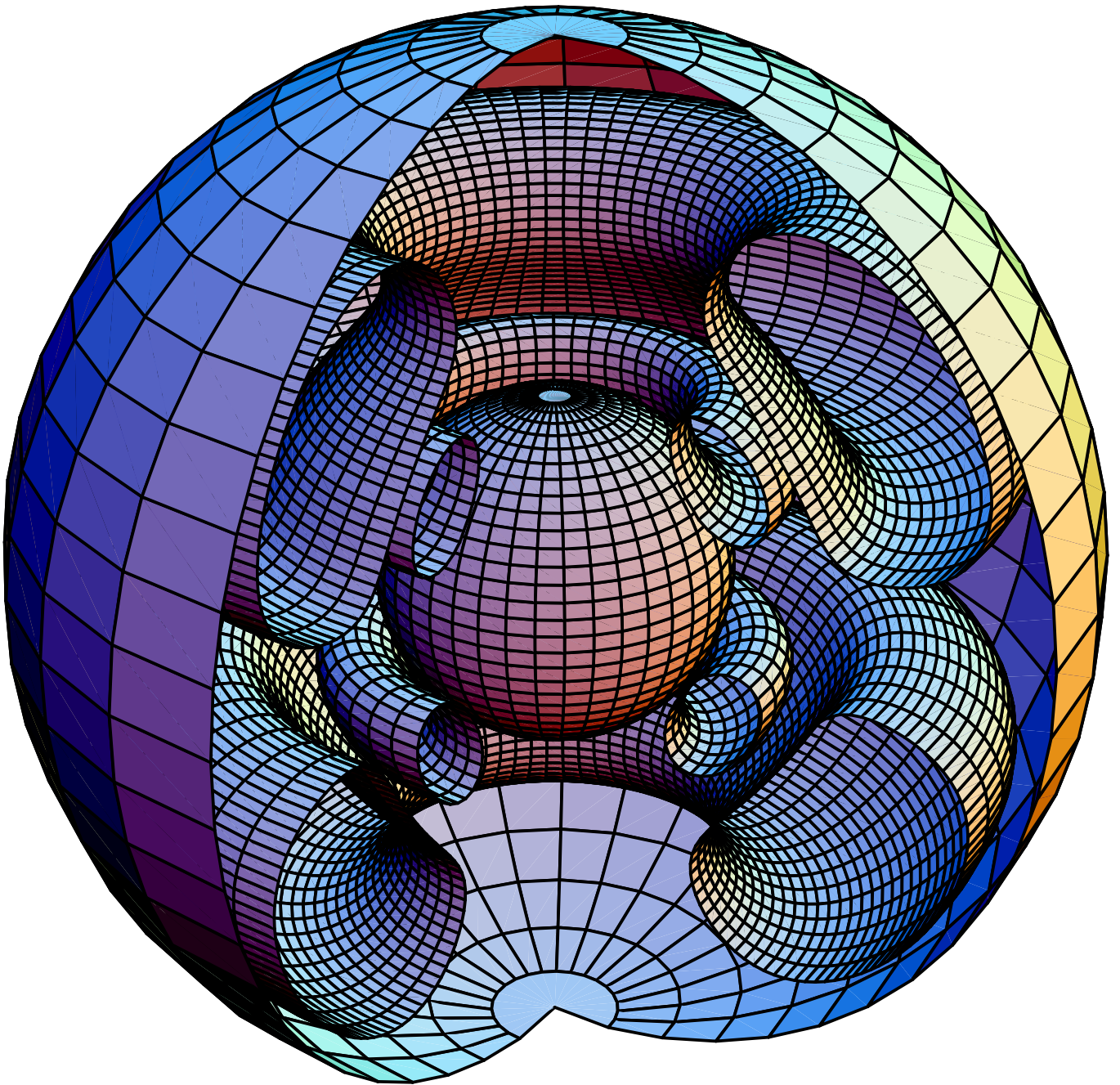
Fig. 1. Stream lines of meridional circulation in a rotating 20 $M_\odot$ model with solar metallicity and v_{ini} = 300 km s^{-1} at the beginning of the H–burning phase (see text). The streamlines are in the meridian plane. In the upper hemisphere on the right section, matter is turning counterclockwise along the outer stream line and clockwise along the inner one. The outer sphere is the star surface and has a radius equal to 5.2 $R_\odot$. The inner sphere is the outer boundary of the convective core. It has a radius of 1.7 $R_\odot$.

The evolution of surface abundances are examined in Sect. 7. In Sect. 8, we discuss the problem of the origin of primary nitrogen and we show how rotation can solve it. The chemical yields in He, CNO and heavy elements are discussed in Sect. 9.

2. Physics of the models

The initial composition is given in Table 1. The composition is enhanced in α–elements. As in Paper VII, the opacities are from Iglesias & Rogers (1996), complemented at low temperatures with the molecular opacities of Alexander (`http://web.physics.twsu.edu/alex/wwwdra.htm`). The nuclear reaction rates are also the same as in Paper VII and are based on the new NACRE data basis (Angulo et al. 1999).

The physics of the present models at $Z = 10^{-5}$ is the same as for models at $Z = 0.004$ (Maeder & Meynet 2001). For rotation, the hydrostatic effects and the surface distortion are included (Meynet & Maeder 1997), so that the T_{eff} given here corresponds to an average orientation angle. The diffusion by shears, which is the main effect for the mixing of chemical

Table 1. Initial abundances in mass fraction.

Element	Initial abundance
H	0.76996750
^{3}He	0.00002438
^{4}He	0.22999812
^{12}C	7.5500e$-$7
^{13}C	0.1000e$-$7
^{14}N	2.3358e$-$7
^{15}N	0.0092e$-$7
^{16}O	67.100e$-$7
^{17}O	0.0300e$-$7
^{18}O	0.1500e$-$7
^{20}Ne	7.8368e$-$7
^{22}Ne	0.6306e$-$7
^{24}Mg	3.2474e$-$7
^{25}Mg	0.4268e$-$7
^{26}Mg	0.4897e$-$7

Fig. 2. Evolution of the angular velocity Ω as a function of the distance to the center in a 15 $M_\odot$ star with $v_{\rm ini} = 300$ km s^{-1} and $Z = 10^{-5}$. $X_{\rm c}$ is the hydrogen mass fraction at the center. The dotted line shows the profile when the He–core contracts at the end of the H–burning phase.

elements, is included (Maeder 1997), with account of the effects of the horizontal turbulence, which reduces the shear effects in regions of steep μ–gradients and reinforces it in regions of low μ–gradients (Maeder & Meynet 2001).

Meridional circulation is the main effect for the internal transport of angular momentum. We use here the expression by Maeder & Zahn (1998) for the vertical component $U(r)$ of the meridional circulation. It is interesting to represent graphically this circulation. Figure 1 illustrates the patterns of the meridional circulation in a 20 $M_\odot$ star at $Z = 0.020$ and initial rotation velocity $v_{\rm ini} = 300$ km s^{-1} on the ZAMS. The figure is symmetrical with respect to the rotation axis, as well with respect to the equatorial plane. The small inner sphere is the edge of the central convective core. The inner tube, in the upper hemisphere, represents an interior cell of the meridional circulation. There is an ensemble of such concentric tubes with different meridional velocities. The motions occur in a meridian plane (i.e. turning around the tube). In the upper hemisphere and around the inner tube, the fluid elements go upward on the inner side of the tube and descend toward the equator on the outer side of the tube ($U(r)$ is positive). The external tube represents an outer circulation cell, due to the Gratton–Öpik term, which is important in the outer stellar layers. This term leads to a negative $U(r)$, which means that, in the upper hemisphere, the fluid goes up on the outer side of the tube and down along the inner side. There also, this tube is one among an ensemble of stream lines turning in the meridian plane.

The mass loss rates are based on the same references as in the paper for the $Z = 0.004$ models (Maeder & Meynet 2001) and in particular on the data by Kudritzki & Puls (2000) for the OB stars. Of course, the strong reduction of the mass loss rates with metallicity for stars below 60 $M_\odot$ makes the mass loss rather unimportant for the metallicity $Z = 10^{-5}$ considered here, as illustrated by Table 1 which shows the values of the final masses. We account for the effects of rotation on the mass loss rates, according to the standard stellar wind theory applied to a rotating star (Maeder & Meynet 2000). The net result is
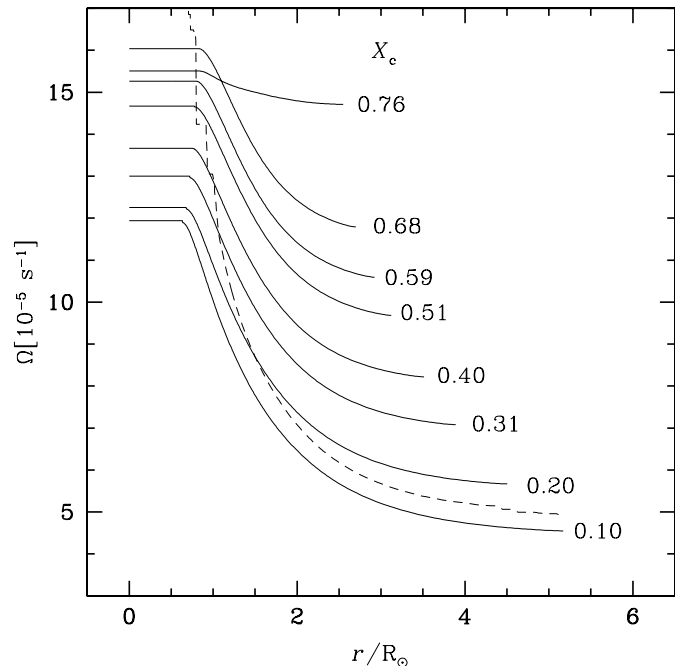
that the very massive stars with initial $M \geq 60\ M_\odot$ may still experience significant mass loss as shown in Table 1, if they rotate very fast.

Star models with initial masses superior or equal to 9 $M_\odot$ were computed up to the end of the carbon–burning phase. Star models with masses between 2 and 7 $M_\odot$ were evolved beyond the end of the He–burning phase through a few thermal pulses during the AGB phase.

3. The evolution of the internal rotation and meridional circulation

There are remarkable differences in the internal distributions of the angular velocity $\Omega(r)$ depending on the stellar metallicity Z. This was already suggested in Paper VII (Maeder & Meynet 2001), when comparing models at $Z = 0.004$ and $Z = 0.020$. It is extended here with models at $Z = 10^{-5}$.

These matters are not academic problems ! Indeed, the distribution of $\Omega(r)$ determines for example the mixing of chemical elements, the size of the convective core and therefore the chemical yields. The results in Sects. 8 and 9 below on the chemical yields are a consequence of the distribution of $\Omega(r)$.

Figure 2 shows the evolution of $\Omega(r)$ during the MS phase of a 15 $M_\odot$ at $Z = 10^{-5}$, (this follows the initial convergence of the Ω–profile which is very short, i.e. $\leq 1\%$ of the MS lifetime). We notice that the rotation of the convective core only has a small decrease during the MS phase, much smaller than at higher metallicities. This results from 2 effects. a) The mass loss at $Z = 10^{-5}$ is much smaller than at solar composition and thus less angular momentum is removed from the star. b) As we shall see below, the meridional circulation is very slow in
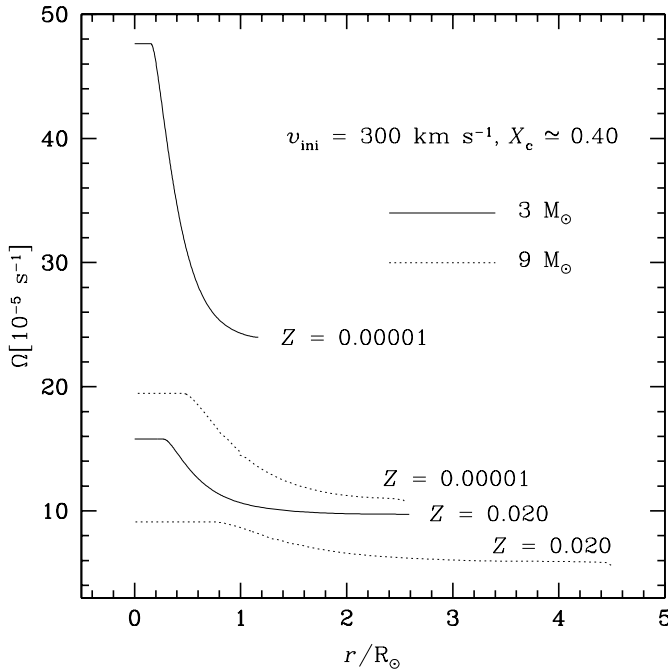
Fig. 3. Variation of the angular velocity Ω as a function of the distance to the center in 3 and 9 $M_\odot$ star models with $v_{\mathrm{ini}} = 300$ km s^{-1} at $Z = 0.020$ and $Z = 10^{-5}$. The mass fraction of hydrogen at the centre $X_{\mathrm{c}} \simeq 0.40$.

Fig. 4. Evolution of $U(r)$ the radial term of the vertical component of the velocity of meridional circulation for a model of 20 $M_\odot$ with $Z = 10^{-5}$ at various stages during the MS phase. X_{c} is the hydrogen mass fraction at the center. The dashed line shows the values of $U(r)$ inside a 20 $M_\odot$ model at $Z = 0.004$ when $X_{\mathrm{c}} = 0.28$.

the outer regions of the models at very low Z and it transports much less angular momentum outwards than in models at solar composition. In view of these remarks, it is likely that massive stars at lower Z have faster spinning cores.

Another significant difference shown by Fig. 2 concerns the gradient of Ω outside the convective cores. Here, the gradients are steeper and they remain significant up to the stellar surface, while at $Z = 0.02$ the Ω–distribution becomes very flat in the external layers, as evolution proceeds (Meynet & Maeder 2000). This difference is well illustrated in Fig. 3, where we notice for the 3 and 9 $M_\odot$ models the much steeper Ω–gradients at lower Z, while the models at $Z = 0.02$ show very flat gradients in the outer layers. The reason for the higher Ω–gradients here are the same as for the faster spinning cores. These higher Ω–gradients imply stronger shears and thus more mixing by shear diffusion, which is the main effect for the outward transport of the chemical species. (The differences in Ω between the 9 and 3 $M_\odot$ models result from the fact that we consider stars with the same v_{ini}, but different radii).

Figure 4 shows an example at $Z = 10^{-5}$ of the evolution of $U(r)$, the vertical component of the velocity of meridional circulation. The size and evolution of $U(r)$ is very different from the case at $Z = 0.02$. At $Z = 0.02$, $U(r)$ takes large negative values particularly in the outer layers. This is due to their low density, which makes a large Gratton–Öpik term $\frac{-\Omega^2}{2\pi G\rho}$ in the expression of $U(r)$, (cf. Maeder & Zahn 1998). At $Z = 10^{-5}$, the large negative values of $U(r)$ have disappeared, $U(r)$ is equal to 10^{-3} cm s^{-1} at the end of the MS phase, while it was 50 times more negative in the corresponding models at $Z = 0.02$ (Meynet & Maeder 2000). The differences do not concern so much the deep interior, but mainly the outer layers.
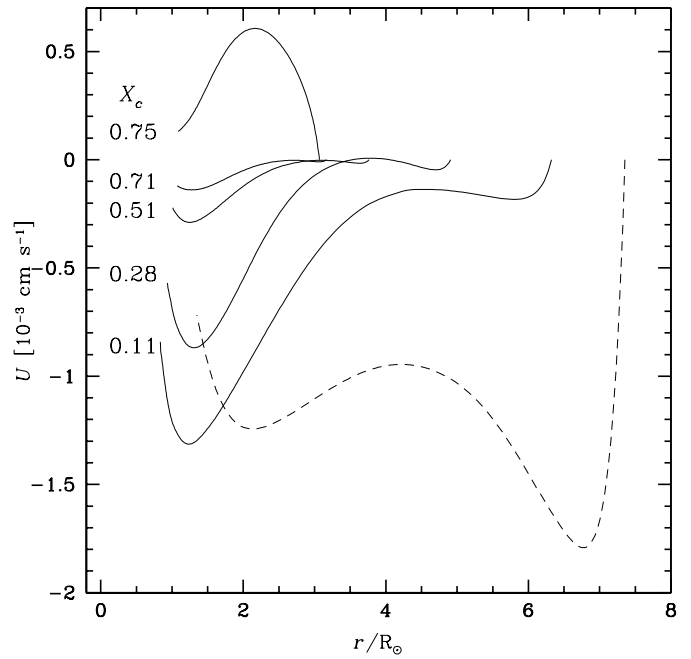
The physical reason of the above differences is the fact that the star is more compact at lower Z and that the density in the outer layers is not as low as at solar composition.

Figure 4 also shows the curious curve for a model at $Z = 0.004$. In the interior, $U(r)$ is about the same as in the present models (and this is true for all Z values). The big external dip of $U(r)$, which was present at $Z = 0.02$ is very much reduced, but still present at $Z = 0.004$, while at $Z = 10^{-5}$ the external dip is fully absent.

The small $U(r)$ in the external layers of the present models is mainly responsible for the presence of an Ω–gradient up to the stellar surface (cf. Fig. 2). Since the mixing of the chemical elements is mainly driven by the shear, the presence of this Ω–gradient in the outer layers enables the large mixing and surface chemical enrichments that are present in the $Z = 10^{-5}$ models.

4. The evolution of the surface rotation velocities

It will probably be a certain time until we are able to observe $v \sin i$ for stars in galaxies with $Z = 10^{-5}$. Nevertheless, these objects have contributed to shape the composition of our universe and they deserve some interest.

Figures 5 and 6 show the evolution of the surface rotational velocities for models with initial masses from 2 to 60 $M_\odot$. Figures 7 and 8 show the corresponding evolution of $\frac{\Omega}{\Omega_{\mathrm{c}}}$. We notice the relative constancy of $\frac{\Omega}{\Omega_{\mathrm{c}}}$ during the MS evolution for stars with mass between 5 and 20 $M_\odot$. The cases of 40 and 60 $M_\odot$ are noticeable as shown by Figs. 5 and 7. These models reach the break–up velocities near the end of the MS phase. This is completely different from the models at $Z = 0.02$, where the rotation becomes very small due to the huge losses of mass
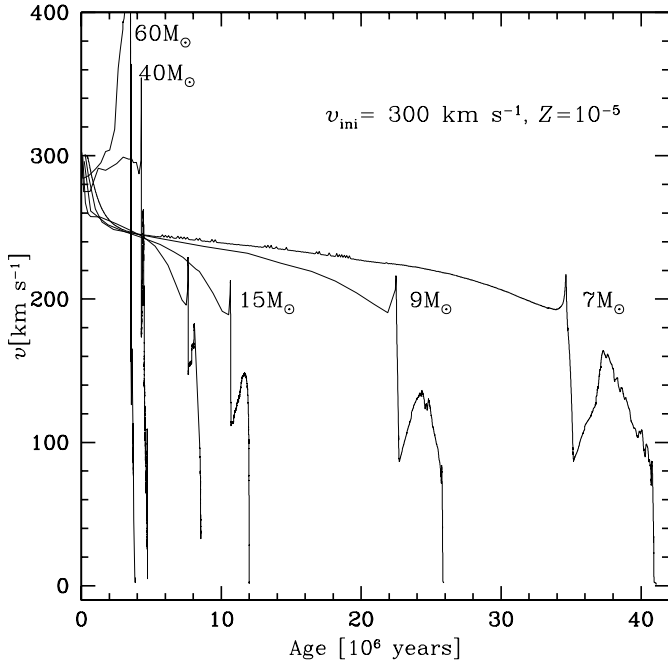
**Fig. 5.** Evolution of the surface equatorial velocity as a function of time for stars of different initial masses with v_{ini} = 300 km s^{-1} and $Z = 10^{-5}$. The track without label corresponds to a 20 $M_\odot$ model.
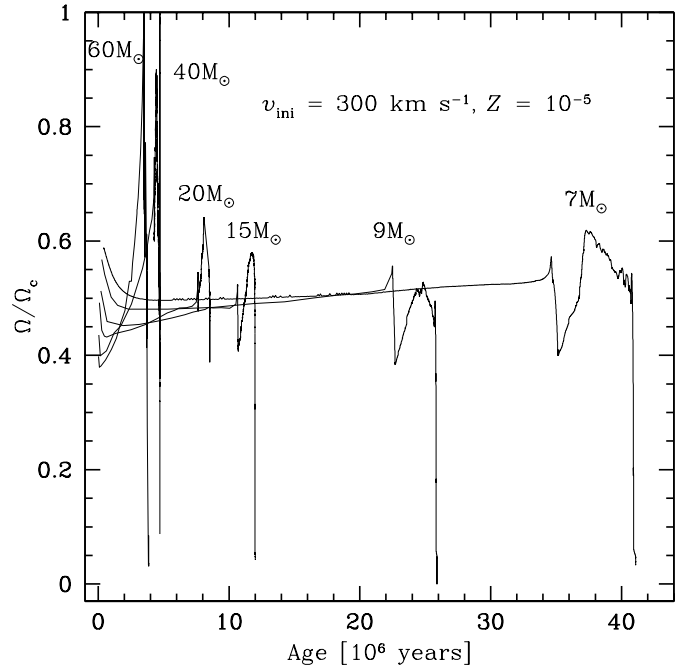
Fig. 7. Evolution of the ratio $\Omega/\Omega_{\mathrm{c}}$ of the angular velocity to the break–up angular velocity at the stellar surface for stars of different masses at $Z = 10^{-5}$.
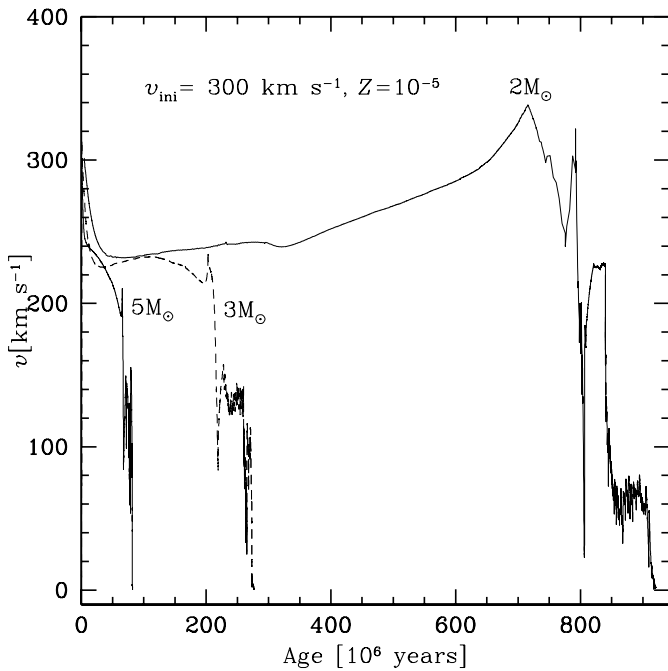
**Fig. 6.** Same as Fig. 5 for a 2, 3 and 5 $M_\odot$ stellar model.
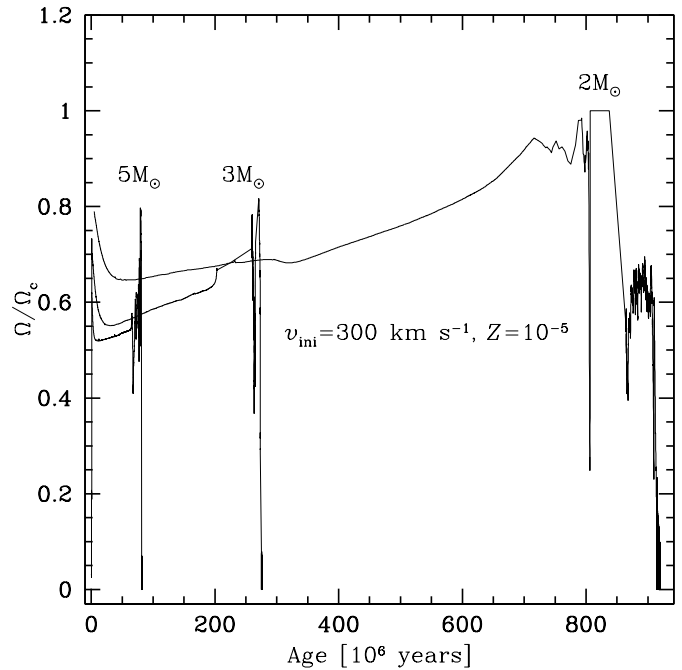
Fig. 8. Same as Fig. 7 for a 2, 3 and 5 $M_\odot$ stellar model.

and angular momentum. Thus, if the initial mass function at low Z extends up to high mass stars, as often supposed, rotation is likely to be a major effect in the course of the evolution of massive stars, since many of them are likely to reach break–up velocities. This would even more be the case for the massive stars which have a blueward evolution as a result of strong internal mixing. Their radii would decrease, thus favouring extreme rotation velocities. We note that for masses between 3

and 20 $M_\odot$, the rotation velocity keeps about constant during the MS phase, before decreasing in the post–MS phases.

Figure 9 clearly illustrates the very different evolution of the rotational velocities of a 60 $M_\odot$ at various metallicities. At low Z like in the models at $Z = 10^{-5}$, the growth of $\frac{\Omega}{\Omega_{\mathrm{c}}}$ is possible because of the very small mass loss and also it is favoured by the outward transport of angular momentum which is much larger for the more massive stars. As shown by Maeder & Meynet (2001), the values of $U(r)$ are more negative for the
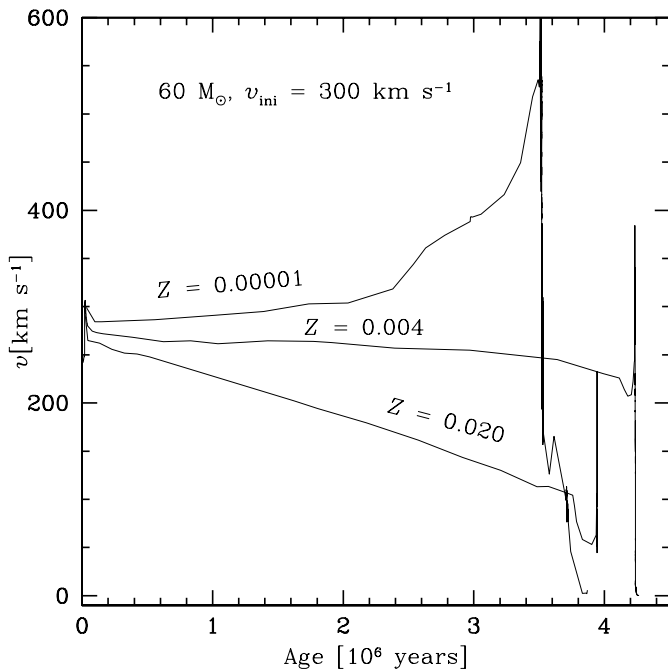
Fig. 9. Evolution of the surface equatorial velocity as a function of time for 60 $M_\odot$ stars with $v_{\rm ini}$ = 300 km s^{-1} at different initial metallicities.

larger stellar masses, due to several facts: lower gravity, higher radiation pressure, larger L/M ratio and especially the lower density. Thus, the outward transport is more efficient.

In view of these results, we may somehow precise our suggestion (Maeder & Meynet 2001) that at very low Z a large fraction of the massive stars reach their break–up velocities. This seems true for the highest masses above about 30 $M_\odot$, but not necessarily for the OB stars below this limit. This question is of high importance, because if the massive stars reach their break–up velocity, most of their evolutionary and structural properties will be affected. For example, they could also lose a lot of mass and produce some Wolf–Rayet (WR) stars. They would have a relatively small remaining mass at the time of the supernova explosion, like their counterparts at solar composition.

For the models of 3 $M_\odot$, as illustrated in Figs. 6 and 8, the rotation velocity remains about constant during the MS phase, while $\frac{\Omega}{\Omega_c}$ increases. For 2 $M_\odot$, we notice a net increase. This particular behavior is due to the different shape of the track of the 2 $M_\odot$ model in the HR diagram (Fig. 10), which mimics the tracks of lower masses dominated by the pp chain. This is well explainable, because at $Z = 10^{-5}$ the CNO cycle is less important than at solar composition, thus the mass limit where the CNO cycle starts dominating over the pp chain is shifted upward. For this model of 2 $M_\odot$, there is no large increase of the radius during the MS evolution and thus rotation keeps higher.

When one examines the evolution of $v \sin i$ during the MS phase for stars of the same mass but different initial velocities, one usually notes at $Z = 0.02$ a so–called velocity convergence (Langer 1998). This is due to the fact that the faster rotating stars lose more mass and thus more angular momentum. In the present models, the mass loss rates are in general very small

(as long as the stars are not at break–up) and thus there is no velocity convergence, i.e. the stars of different initial velocities finish the MS phase with different velocities as illustrated by Table 1.

5. Models with zero rotation

For purpose of comparison, we have computed non–rotating stellar models with the same physical ingredients as for the computation of the rotating ones. The evolutionary tracks are presented in Fig. 10, the lifetimes and various properties of the models are given in Table 2. The models were computed with the Schwarzschild criterion for convection and therefore present the usual differences when compared with models accounting for the effect of overshooting (see Papers V and VII for a more detailed discussion).

With respect to our previous grids of stellar models at solar metallicity (see Paper V), the present models are shifted toward higher effective temperatures, by about 0.15–0.20 dex in log $T_{\rm eff}$. The stars are much more compact than at solar metallicity by nearly a factor two (more precisely by a factor between 1.8–1.9 depending on the initial mass). This is a well known consequence of the low opacities in the outer layers of metal poor stars.

In Paper VII, we noticed that models at $Z = 0.004$ with initial masses between 10 and 12.5 $M_\odot$ were showing a behavior in the HR diagram intermediate between the cases of stars presenting a well developed blue loop and the case of more massive stars, which do not produce any blue loop, but begin to burn their helium in their core at a high effective temperature, while they cross the HR diagram for the first time. Here at $Z = 10^{-5}$, this transition zone covers a broader range of initial masses, from 2 to about 15 $M_\odot$. This is well consistent with grids of stellar models computed by other authors. Indeed a similar broadening in mass for this transition region can be observed in the grids by the Padova group (compare for instance the grids by Fagotto et al. 1994 at $Z = 0.0004$ and that of Girardi et al. 1996 at $Z = 0.0001$).

From Fig. 10, one sees that the 20 $M_\odot$ model does not reach the red supergiant phase at least before the end of the C–burning phase. This feature is also present in zero metallicity stellar models (see e.g. Marigo et al. 2001), but for pop III models, it extends over a broader range of initial masses (from ~10 to ~40 $M_\odot$). Finally, let us note that, when the metallicity decreases, the mass limit for the helium flash decreases (see also Marigo et al. 2001). This is a consequence of the higher central temperatures reached in metal poor stars. Typically a 2 $M_\odot$ model at solar metallicity, computed with the same physical ingredients as used in the present work, undergoes He–flash, while the corresponding model at $Z = 10^{-5}$ ignites helium in a non–degenerate environment.

6. HR diagram, mass–luminosity relations and lifetimes

The effects of rotation at $Z = 0.020$ have already been discussed in Talon et al. (1997), Denissenkov et al. (1999), Heger et al. (2000a), Heger & Langer (2000),
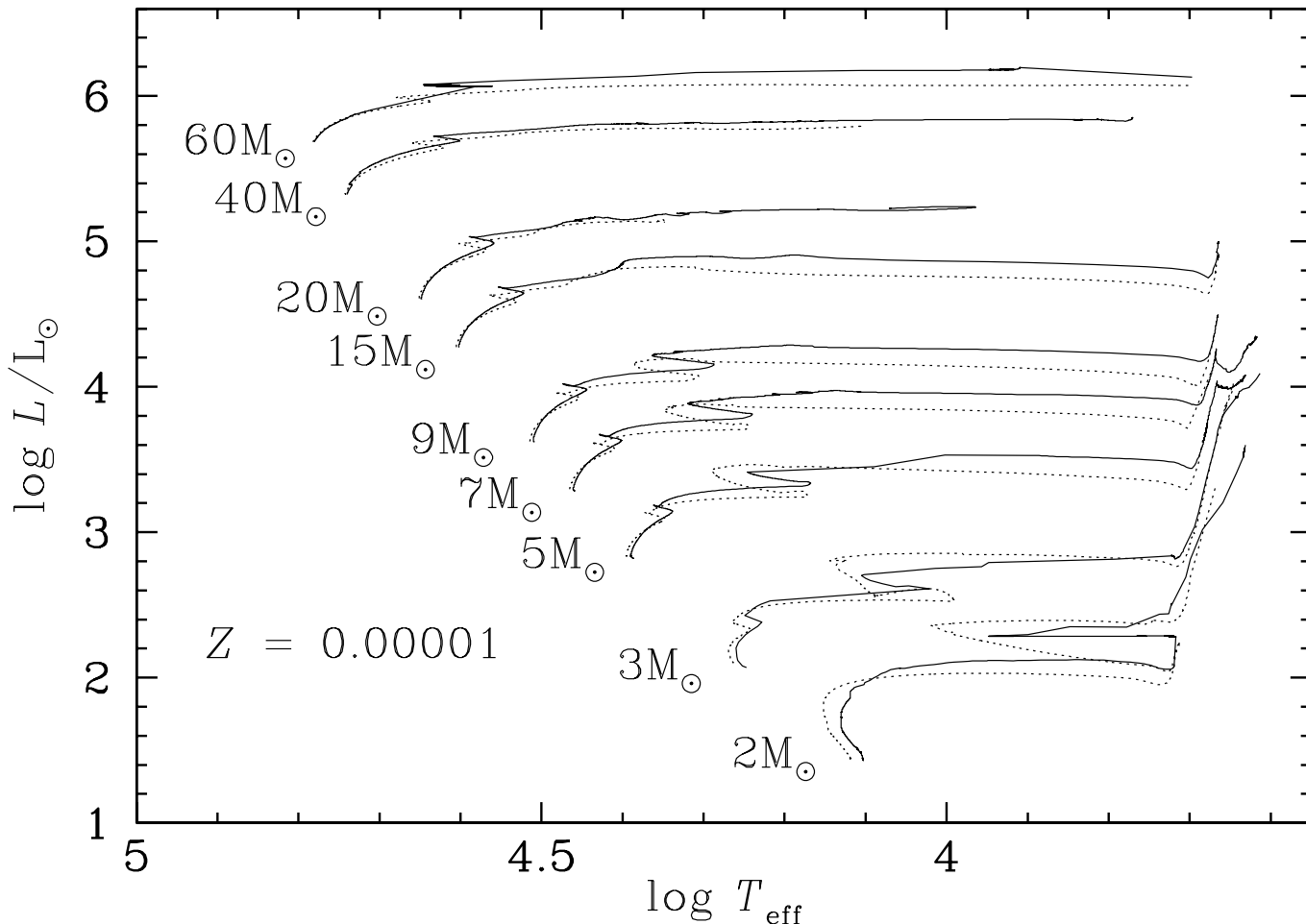
Fig. 10. Evolutionary tracks for non–rotating (dotted lines) and rotating (continuous lines) models for a metallicity $Z = 10^{-5}$. The rotating models have an initial velocity v_{ini} of 300 km s^{-1}.

Meynet & Maeder (2000). At the metallicity of the Small Magellanic Cloud, the effects of rotation have been discussed by Maeder & Meynet (2001). Let us very briefly recall the most important effects of rotation:

- The Main Sequence (MS) evolutionary tracks with rotation are extended toward lower effective temperatures and reach higher luminosities at the end of the MS phase than their non–rotating counterparts. In that respect rotation acts as a moderate overshoot.
- The MS lifetimes increase with rotation, typically by about 10% for a 20 $M_\odot$ model with an average rotational velocity on the MS corresponding to the observed ones.
- For a given value of the initial mass and metallicity, the evolutionary tracks may be different, due to different initial rotational velocities. Even for a given initial rotation, the tracks may appear different depending on the angle of view, since the polar regions of a rotating star are in general hotter than the equatorial ones (cf. Maeder & Peytremann 1970). This induces some scatter in the position of the end of the MS phase in the HR diagram.
- The theoretical period–luminosity relation for the Cepheids is changed by rotation. A Cepheid, at a given position in the HR diagram, if originating from a rotating progenitor, will pulsate with a longer period than a Cepheid having a non–rotating progenitor.
- The evolution toward the red supergiant phase is favoured by rotation. Rotation also facilitates the formation of Wolf–Rayet stars.
- The surface abundances are modified.

We shall see that the models at the very low metallicity $Z = 10^{-5}$ present some striking differences with respect to what happens at higher metallicities: in particular, rotation implies smaller main sequence lifetimes and rotation does not favour the evolution toward the red supergiant stage (at least for the range of initial velocities explored here).

6.1. The HR diagram

For most of the stellar models, we computed the rotating tracks for an initial velocity $v_{ini} = 300$ km s^{-1}. This value of v_{ini} corresponds to a mean velocity $\bar{v}$ during the MS between 226 and 240 km s^{-1} for initial masses below 20 $M_\odot$ (see Table 2). These values are close to the mean rotational velocities observed for OBV type stars at solar metallicity, which are between 200–250 km s^{-1}. For more massive stellar models at $Z = 10^{-5}$ the average velocities are higher. This results essentially from the

Table 2. Properties of the stellar models at the end of the H–burning phase, at the end of the He–burning phase and at the end of the C–burning phase or during the thermal pulse–AGB phase. The masses are in solar mass, the velocities, in km s^{-1} and the lifetimes, in million years. The abundances are in mass fraction. The abundance ratios are normalized to their initial values, which are, in mass fraction, $(N/C)_{ini} = 0.309$ and $(N/O)_{ini} = 0.035$.

			End of H–burning					End of He–burning					End of C–burning				
M	v_{ini}	$\bar{v}$	t_H	v	Y_s	N/C	N/O	t_{He}	v	Y_s	N/C	N/O	M_{fin}	v	Y_s	N/C	N/O
60	0	0	3.883	0	0.23	1.00	1.00	0.332	0	0.23	1.00	1.00	59.57	0	0.23	1.00	1.00
	300	327	3.513	545	0.35	64.2	25.8	0.345	2	0.47	126	49.8	50.42	5	0.51	145	63.0
40	0	0	4.974	0	0.23	1.00	1.00	0.419	0	0.23	1.00	1.00	39.86	0	0.23	1.00	1.00
	300	289	4.279	355	0.25	80.8	14.3	0.436	21	0.28	123	19.1	38.61	4	0.30	139	22.4
20	0	0	8.773	0	0.23	1.00	1.00	0.886	0	0.23	1.00	1.00	19.97	0	0.23	1.00	1.00
	200	157	7.445	139	0.23	12.8	4.89	0.978	8	0.23	21.3	6.55	19.97	1	0.26	45.2	11.6
	300	240	7.624	228	0.23	28.6	7.20	0.902	81	0.24	54.2	10.4	19.97	75	0.24	54.8	10.6
	400	325	7.737	338	0.23	69.1	9.23	0.932	155	0.27	150	16.6	19.90	208	0.27	153	17.3
15	0	0	12.12	0	0.23	1.00	1.00	1.473	0	0.23	1.00	1.00	14.99	0	0.30	42.3	19.5
	300	234	10.65	212	0.23	21.9	6.74	1.281	111	0.24	53.6	11.3	14.98	2	0.29	126	23.2
9	0	0	25.12	0	0.23	1.00	1.00	3.285	0	0.23	1.00	1.00	8.998^a	0	0.24	34.5	15.5
	200	151	22.03	128	0.23	5.45	3.16	3.414	72	0.23	24.6	8.00	8.997	1	0.26	79.3	18.0
	300	230	22.50	212	0.23	79.5	10.5	3.040	73	0.23	107	12.0	8.997^a	2	0.27	234	23.4
	400	307	22.77	294	0.23	365	13.7	3.612	86	0.24	477	17.4	8.997^a	2	0.27	579	25.7
													AGB phase				
													M_{fin}	Y_s	C	N	O
7	0	0	38.28	0	0.23	1.00	1.00	5.917	0	0.23	1.00	1.00	6.999	0.24	2.5E-7	2.4E-6	4.9E-6
	300	229	34.66	209	0.23	78.6	9.67	5.576	74	0.24	160	12.9	6.998	0.36	1.7E-3	7.0E-4	6.6E-4
5	0	0	70.71	0	0.23	1.00	1.00	14.38	0	0.23	1.00	1.00	5.000	0.24	2.5E-7	2.2E-6	5.0E-6
	300	226	65.69	198	0.23	16.3	5.32	13.61	94	0.24	68.2	12.7	4.996	0.34	7.5E-4	1.0E-3	3.9E-4
3	0	0	200.6	0	0.23	1.00	1.00	50.22	0	0.23	1.00	1.00	2.990	0.27	2.9E-7	1.7E-6	5.5E-6
	300	229	208.0	228	0.23	26.9	6.97	52.52	29	0.26	177	15.8	2.910	0.29	1.3E-5	7.4E-4	2.0E-4
2	0	0	637.5	0	0.23	1.00	1.00	109.3	0	0.24	4.47	2.59	2.000	0.25	3.5E-7	1.0E-6	6.3E-6
	300	251	688.3	318	0.23	3.27	2.29	107.8	9	0.28	257	10.8	1.863	0.29	6.2E-8	6.0E-6	5.7E-6

^{a} Models at the beginning of the C–burning phase.

larger outward transport of angular momentum by circulation in more massive stars (see Sect. 4 and Maeder & Meynet 2001).

Figure 10 shows the evolutionary tracks of non–rotating and rotating stellar models for initial masses between 2 and 60 $M_\odot$. The effective temperatures plotted correspond to an average orientation angle (see also Paper I). At the beginning of the evolution on the ZAMS, rotational mixing has no impact on the structure, since the star is homogeneous. At this stage, only the hydrostatic effects of rotation are present, i.e. the effects due to the centrifugal acceleration term in the hydrostatic equilibrium equation. As is well known, these effects shift the ZAMS position toward lower values of L and T_{eff} (see e.g. Paper I). From Fig. 10, one sees that the less massive the star, the greater the shift. This results from the facts that, for a given v_{ini}, the lower the initial mass, the greater the ratio of the centrifugal force to the gravity. Indeed this ratio, equal to $\frac{v_{ini}^2}{R}\frac{R^2}{GM}$, varies as about $1/M^\alpha$ with α equal to about 0.4.

As was the case at higher metallicities, the MS width is increased by rotation. Rotational mixing brings fresh H–fuel into the convective core, slowing down its decrease in mass during the MS. A more massive He–core is produced at the end of the H–burning phase, which favours the extension of the tracks toward lower effective temperatures. Rotational mixing also transports helium and other H–burning products (essentially nitrogen) into the radiative envelope. The He–enrichment lowers the opacity. This contributes to the more rapid increase of the stellar luminosity during the MS phase and limits the redwards motion in the HR diagram.

The widening of the MS produced by rotation mimics the effect of an overshoot beyond the convective core (see Talon et al. 1997, Paper VII). Since the observed width of the MS has often been taken to parameterize the size of the convective core, the above argument shows that rotating models tend to decrease the amplitude of the overshoot necessary to reproduce the observed MS width.

Figure 11 shows the evolutionary tracks of 20 $M_\odot$ models for different initial velocities and metallicities during the H–burning phase. One sees that the extension of the MS due
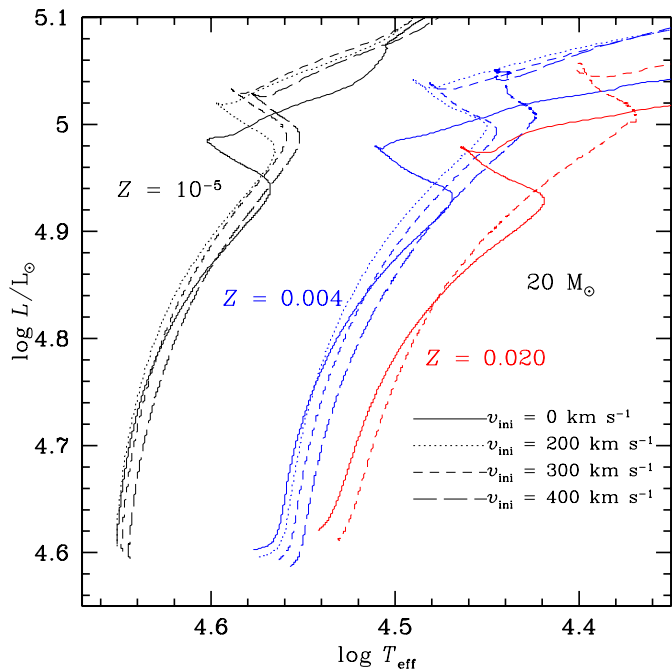
Fig. 11. Evolutionary tracks for rotating 20 $M_\odot$ models with different initial velocities and various initial metallicities. The initial velocities $v_{\rm ini}$ are indicated. See Table 1 for more details on the models at $Z = 10^{-5}$.

to rotation decreases when the metallicity decreases. This results from the smaller increase of the He–core due to rotation at low Z. Typically, at the end of the MS at $Z = 10^{-5}$, the helium core mass in the rotating 20 $M_\odot$ model ($v_{\rm ini} = 300$ km s^{-1}) is greater by 11% with respect to its value in the non–rotating model. The corresponding increase at $Z = 0.004$ is 23%. The reason for this difference is the following one. When rotation brings fresh hydrogen fuel, in the core, it brings also carbon and oxygen which act as catalysts in the CNO burning. These catalyst elements are of course in much lower abundances at $Z = 10^{-5}$ than at $Z = 0.004$ and thus the core enhancement is less pronounced.

At $Z = 0.004$, the rotating star models with initial masses between 9 and ~25 $M_\odot$, are evolving, after the MS phase, much more rapidly toward the red supergiant stage (RSG) than the non–rotating models, in agreement with the observed number ratio of blue to red supergiants in the Small Magellanic Cloud cluster NGC 330 (Maeder & Meynet 2001). As was extensively discussed, the balance between the blue and the red is very sensitive to many effects. At the very low metallicity considered here, rotation does not succeed in producing red supergiants, at least for the range of initial rotational velocities explored. The dominant reason appears to be the smaller He–cores produced at lower Z and the fact that the growth of this core due to rotation is smaller than at higher Z. In terms of the discussion by Maeder & Meynet (2001), this reduces the central potential enough to keep a blue location during the whole He–burning phase, and the amount of helium diffused in the region of the shell is unable to compensate for the smaller core. Only, during the very last stages in the C–burning phase, when the

core heavily contracts, does the central potential grow enough to produce a red supergiant.

The rotating models do not present any well developed blue loop, except in the case of the 2 $M_\odot$ model. In that respect the situation is similar to the case of the non–rotating models (see Sect. 5 above). Interestingly, we note that the rotating models, with initial mass below 7 $M_\odot$, evolve redwards during the AGB–phase. This a consequence of the third dredge–up, which brings at the surface carbon and oxygen synthesized in the He–burning shell, as well as primary nitrogen built up in the H–burning shell (see Sects. 7 and 8). The important enhancements of these elements at the surface make the star to behave as a more metal rich star and thus push it to a redder location in the HR diagram.

In the present grid no model enters the Wolf–Rayet phase. At the end of the C–burning phase, the mass fraction of hydrogen at the surface of the rotating 60 $M_\odot$ model is still important (~0.48), although much lower than at the surface of the corresponding non–rotating model (~0.77). It is likely that more massive or faster rotating star models may enter the Wolf–Rayet phase before central He–exhaustion.

6.2. Masses and mass–luminosity relations

Table 2 presents some properties of the models. Columns 1 and 2 give the initial mass and the initial velocity $v_{\rm ini}$ respectively. The mean equatorial rotational velocity $\bar{v}$ during the MS phase is indicated in Col. 3. The H–burning lifetimes $t_{\rm H}$, the equatorial velocities v, the helium surface abundance $Y_{\rm s}$ and the surface ratios N/C and N/O at the end of the H–burning phase and normalized to their initial values are given in Cols. 4 to 8. The Cols. 9 to 13 present some properties of the models at the end of the core He–burning phase; $t_{\rm He}$ is the He–burning lifetime. Some characteristics of the last computed models are given in Cols. 14 to 18; $M_{\rm fin}$ is the final stellar mass. For stars with initial mass superior or equal to 9 $M_\odot$, the final stage corresponds to the end of the C–burning phase. For the lower initial mass stars, it corresponds to the beginning of the Thermal Pulse AGB (TP–AGB) phase. Typically the rotating 3 $M_\odot$ model was computed until the fifth thermal pulse. For the intermediate mass stars, the mass fractions of carbon (C), oxygen (O) and nitrogen (N) at the surface of the stars are given.

Rotation, by enhancing the luminosity and lowering the effective gravity, increases the mass loss rates (Maeder & Meynet 2000). As a consequence, the final masses of the rotating models are smaller. At the metallicity $Z = 10^{-5}$, except for the 60 $M_\odot$ model, the effects of rotation on the final stellar masses are very weak (see Table 2).

In general, rotation makes the star overluminous for their actual masses. Typically for $v_{\rm ini} = 300$ km s^{-1}, the luminosity vs. mass (L/M) ratios at the end of the MS are increased by 10–14% for stars in the mass range from 3 to 40 $M_\odot$. This results essentially from the He diffusion in the radiative envelope which lowers the opacity and makes the star overluminous. In the 60 $M_\odot$ model, mixing is particularly efficient and the increase of the L/M ratio amounts to 23%. For the 2 $M_\odot$ model, the L/M ratio is decreased in the rotating model, by 6–7%.

In this last case, the convective core during the H–burning phase disappears very early, when the mass fraction of hydrogen in the center is still high ($X_c = 0.52$ in the $v_{ini} = 300$ km s^{-1} model). This puts farther away from the surface the region where helium is produced and thus slows down the helium diffusion in the outer envelope.

The increase of L/M, due to rotation, at $Z = 10^{-5}$ are in general inferior to those obtained at $Z = 0.004$, which are between 15–22% (Maeder & Meynet 2001). This is mainly a consequence of the following fact: at $Z = 10^{-5}$, the increase of the H–burning convective core due to rotation is inferior to that obtained at $Z = 0.004$ for the same value of v_{ini}.

6.3. Lifetimes

Generally we can say that the MS lifetime duration is affected by rotation at least through three effects:

– 1) Rotation increases the quantity of hydrogen burnt in the core. This increases the MS lifetime.
– 2) The hydrostatic effects of rotation make a star of a given initial mass to behave as a non–rotating star of a smaller initial mass. This tends to increase the MS lifetime.
– 3) Rotation increases the helium abundance in the outer radiative envelope. This tends to make the star overluminous with respect to its non–rotating counterpart and thus to reduce the MS lifetime.

When the metallicity decreases, the effect number 3 tends to become the most important one.

This can be seen from a detailed comparison of the tracks in Fig. 11. Indeed the evolutionary tracks for our rotating 20 $M_\odot$ models ($v_{ini} = 300$ km s^{-1}) become overluminous with respect to the non–rotating tracks at an earlier stage for lower metallicities. This mainly results from the fact that when the metallicity decreases, rotational mixing is more efficient (see Sect. 3). Also, at lower Z, the stars are more compact and therefore the timescale for mixing, which is proportional to the square of the radius, decreases. This favours the helium diffusion in the outer envelope. The diffusion of hydrogen into the core, which would increase the MS lifetime, is not really affected, because hydrogen just needs to migrate over the convective core boundary to be engulfed into the core. One notes also that for given values of the equatorial velocity and of the initial mass, the ratio Ω/Ω_c of the angular velocity to the break–up velocity decreases whith the metallicity. Thus the hydrostatic effects, which usually make the star fainter, are in general smaller at lower Z.

As a consequence of the above effects, at $Z = 10^{-5}$, the MS lifetimes are decreased by about 4–14% for the mass range between 3 and 60 $M_\odot$ when v_{ini} increases from 0 to 300 km s^{-1} (cf. Table 2).

We notice that the rotating 2 $M_\odot$ model has a longer MS phase than its non–rotating counterparts, in contrast with what happens for higher initial mass stars. This is because, when the initial mass decreases, the hydrostatic effects become more and more important (see Fig. 10).

For what concerns the effects of rotation on the He–burning lifetime, let us simply say that when v_{ini} increases from 0 to
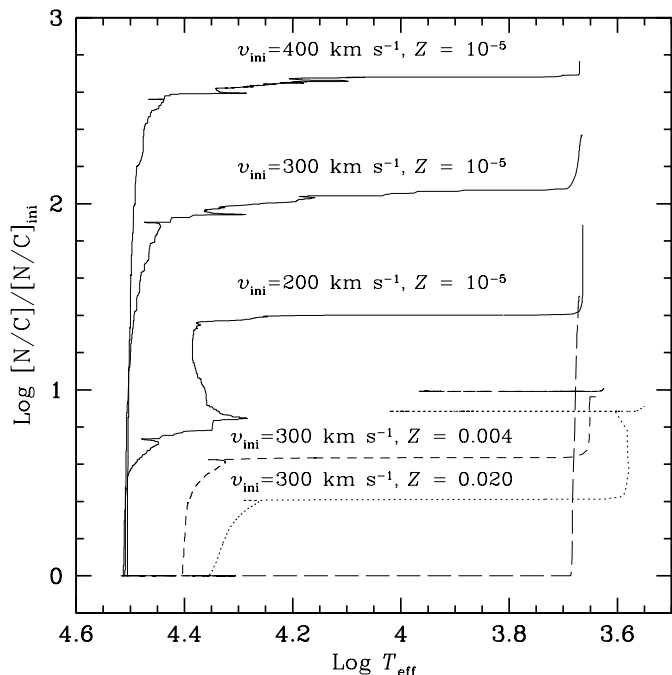
Fig. 12. Evolution as a function of log T_{eff} of the abundance ratio N/C where N and C are the surface abundances of nitrogen and carbon respectively. The abundance ratios are normalized to their initial values. The tracks are for 9 $M_\odot$ for different values of the metallicity, Z, and rotation. The long–dashed line, at the bottom, corresponds to a non–rotating 9 $M_\odot$ stellar model at $Z = 10^{-5}$.

300 km s^{-1}, the changes in the He–burning lifetimes are inferior to 10%.

7. Evolution of the chemical abundances at the surface

Figure 12 shows the evolution of the N/C ratios in models of rotating stars with 9 $M_\odot$ for the initial $Z = 0.02$, 0.004 and 10^{-5}. Values for other stellar masses may be found in Table 2.

At zero rotation, for any Z and any masses there is no enrichment during the MS phase (except at $Z = 0.02$ for $M \geq 60$ $M_\odot$ due to very high mass loss). At 9 $M_\odot$ for an initial rotation of 300 km s^{-1}, we notice an increase of the N/C ratio already during the MS phase. In fact most of the increase in N/C is in general built during the MS phase, and this results from the steeper Ω–gradients and greater compactness. The *relative* growths of the N/C ratio do not change very much from models with $Z = 0.02$ to models with $Z = 0.004$, however there is an increase by two orders of a magnitude for $Z = 10^{-5}$. Of course this large N/C enhancement is accompanied by a small enrichment in helium at the surface, typically of a few hundredths as shown by Table 2. Figure 12 illustrates the fact we find throughout this work, i.e. that the various effects of rotation on the internal structure, the surface composition and the yields are in general much higher at lower metallicities.

In Fig. 12, we notice for $Z = 10^{-5}$ an increase by a factor 4.5 of the N/C ratio for an increase of 100 km s^{-1} of the initial rotation. As illustrated by Table 2, during the He–burning phase the rotation velocities become all the same whatever the

initial rotational velocities. Thus, in the He–burning phase we may have very different surface chemical compositions for actually similar rotation velocities. This is likely true for all stellar masses where fast rotation is present, but the effect is in general larger for larger masses.

Curiously enough, at very low Z the fast rotating stars of intermediate masses which reach the TP–AGB phase (this occurs for $M \leq 7\,M_\odot$) get a higher Z during this phase due to their enrichment in CNO elements. As an example, a $7\,M_\odot$ has a $X(\text{CNO}) = 3.1 \times 10^{-3}$ which is 430 times the initial CNO content. Thus very low Z stars may become higher Z stars near the end of their evolution. This might also affect the composition of planetary nebulae in low Z regions.

8. Primary nitrogen production

8.1. Brief recalls on the nitrogen synthesis

Nitrogen is mainly produced in the CN branch of the CNO cycles within H–burning stellar zones (see Clayton 1983; Arnett 1996). More precisely, three reactions occur to transform ^{12}C to ^{14}N: ^{12}C$(p, \gamma)^{13}$N$(\beta^+, \nu)^{13}$C$(p, \gamma)^{14}$N. Nitrogen can also be produced in the ON cycle by transformation of ^{16}O, but at a much slower rate. The reaction ^{14}N$(p, \gamma)^{15}$O which depletes nitrogen has a relatively low cross section enabling ^{14}N to accumulate with time. Thus, ^{14}N is usually the daughter element, hence a secondary element, of the CNO initially present in stars.

Nitrogen is said to be primary (Talbot & Arnett 1974), if it is formed in a star not from the initial CNO elements, but from the hydrogen and helium. Of course, the reactions forming primary nitrogen are those mentioned above, but the sequence of events is different: the formation of primary nitrogen implies firstly the synthesis of some ^{12}C by the 3α–reaction in a helium burning region, then this new ^{12}C needs to be transported in an hydrogen burning region, where the CNO cycle will convert it to nitrogen. Thus, primary nitrogen is likely to be formed in stars with a He–burning core and a CNO burning shell, provided there is some transport mechanism between the two. The absence of such transport is the main reason why current models do not produce in general any primary nitrogen.

If ^{14}N is of primary origin, the ^{14}N–abundance is proportional to that of the other primary heavy elements. While if nitrogen is secondary, the increase in the abundance of ^{14}N is proportional to the initial CNO content and thus in the chemical history of a galaxy the ^{14}N–content will be proportional to the square of the CNO and metal content. These different behaviors provide the basic test for ascertain the primary or secondary origin of nitrogen.

The observations point toward the need of primary nitrogen sources at low metallicities (see below). The main problem is that the stellar models, unless ad hoc hypothesis are made, do not currently predict any primary nitrogen. This suggests that some physical process may be missing in the stellar models.

There are two other related problems. At solar metallicities, the observations do not suggest the production of primary nitrogen. Thus, a global question is how is changing the respective efficiencies of the primary and secondary ^{14}N productions during the evolution of galaxies. The other question concerns the relative importance of massive and intermediate mass stars in the production of primary and secondary nitrogen. This point is important in relation for the interpretation in terms of the star formation history the N/O ratios observed at high redshifts (Pettini et al. 1995; Lu et al. 1998). Nitrogen, primary and secondary, is produced in the longest and main evolutionary phases. As long as its production is not well understood, we may doubt of the correctness of the models for these main phases of stellar evolution.

8.2. The observations of the N/O ratio

There are several kinds of evidences in favour of primary nitrogen in the early phases of the evolution of galaxies.

1) An indication of primary nitrogen is provided by the study of the N/O ratio in low metallicity stars of the galactic halo. The "discovery" of primary nitrogen was made by Edmunds & Pagel (1978) in a study of the N/O ratio in such stars and in some external galaxies. Following this work, others authors (Barbuy 1983; Tomkin & Lambert 1984; Matteucci 1986; Carbon et al. 1987; Henry et al. 2000) have shown that the ratio N/O of nitrogen to oxygen remains constant with a plateau at log N/O $\simeq -1.7$ in the early evolution of the Galaxy, thus implying a primary origin of nitrogen. The limit in metallicity above which secondary production of nitrogen becomes important is difficult to fix with precision, since the transition is progressive. It is around $12 + \log \text{O/H} = 7.8$ to 8.2 according to Henry et al. (2000; cf. also Izotov & Thuan 1999). Since for the Sun one has $12 + \log \text{O/H} = 8.9$, this means at a metallicity Z equal to $Z_\odot/12$ to $Z_\odot/5$. Above this limit, the N/C and N/O ratios grow rapidly, implying that nitrogen is essentially a secondary element. It is not known whether the primary production stops completely for Z values higher than the above limit. A good way to check it would be to measure the sum of CNO elements in planetary nebulae of the SMC, LMC and Galaxy, to see whether this sum is higher than the initial local CNO content of these galaxies.

2) A very compelling evidence for primary ^{14}N is provided by the study of the N/O ratios in ionized HII regions of blue compact dwarf galaxies (Thuan & Izotov 1995; Kobulnicky & Skillman 1996; Izotov & Thuan 1999; Izotov & Thuan 2000). These HII regions also show a plateau of N/O at log N/O $\simeq -1.7$ below $12 + \log \text{O/H} \simeq 8.0$, while above this limit the N/O ratio is a steeply growing function of O/H, as due to the secondary production of nitrogen. An example of a low metallicity galaxy is IZw 18, which has the lowest known metallicity (1/50 of solar), and which shows indications of primary nitrogen (Kunth et al. 1995; Izotov & Thuan 1999). The study of the N/O ratio in spiral galaxies by van Zee et al. (1998) well confirms the same result, with the difference that the authors find a plateau below $12 + \log \text{O/H} = 8.45$, i.e. for abundance of heavy elements less than 1/3 solar.

A problem was that some low Z damped Lyα systems have N/O ratios lower than those observed in the HII regions of blue compact dwarf galaxies of the same Z (Pettini et al. 1995). However, the apparent discrepancy has been resolved

by models of damped Lyα systems which account for both ionized and neutral regions (Izotov et al. 2001).

3) Another argument for primary nitrogen production comes from the observed gradient of N/O in spiral galaxies. If nitrogen is purely a secondary element, the N/O gradient should be identical to that of O/H. In general, the N/O gradients tend to be shallower than the O/H gradients (Vilchez & Esteban 1996). The various data on the galactic gradients of N/O (Rudolph et al. 1997; Garnett et al. 1997; Ferguson et al. 1998; Henry & Worthey 1999) generally show that the N/O gradient is relatively flat at low metallicity Z, which supports the conclusion that the production of nitrogen is dominated by primary processes at low Z, while at solar or higher Z the similarity of the N/O and O/H gradients support the view that nitrogen is secondary.

The situation is rather confused concerning the masses of the stars responsible for the injection of primary nitrogen. There are authors supporting the origin of primary nitrogen in massive stars (Matteucci 1986; Thuan & Izotov 1995; Izotov & Thuan 1999; Izotov & Thuan 2000). Their main argument is the low scatter of the observed N/O ratios at low Z. Indeed, if nitrogen is synthesized in massive stars, there is no time delay between the injection of nitrogen and oxygen and thus a rather small scatter would result. On the contrary, if the primary nitrogen is made in intermediate mass stars, the N/O ratio increases with time, since these stars release their nitrogen much later than massive stars do eject their oxygen. This would lead to a larger scatter in the observations, because galaxies are observed at various stages of their evolution. Izotov & Thuan (1999) suggest also that because of the intermediate mass star delay, the faster evolving massive stars must be a significant source of primary nitrogen in order to raise the log(N/O) ratio to the observed plateau at $12 + \lg(\text{O/H}) \sim 7.2$, a metallicity they assume to correspond to a galactic age too short to allow nitrogen ejection by the intermediate masses.

The situation may be not so clear, because some studies found that a significant scatter does exist (Garnett 1990; Skillman et al. 1997). Also, Henry et al. (2000) have calculated chemical evolution models which support the view that intermediate mass stars between 4 and 8 $M_\odot$, with an age of about 250 Myr, are likely to dominate the nitrogen production.

What can we deduce if we accept the fact that the N/O values show a great scatter at fixed value of O/H? A possibility might be that the observed scatter occurs because we are observing a large sample of HII regions in various stages of oxygen and nitrogen enrichments. This picture implies that most observed data should have relatively high N/O values with fewer points, representing those objects experiencing sudden oxygen enrichment, located below the bulk of data, since presumably bursts are followed by relatively long periods of quiescence, with relatively higher N/O ratios.

The reality looks different. The distribution of points in N/O vs. O/H plane reveals that most points seem to be clustered at relatively low values. This suggests that the "equilibrium" or unperturbed locus where most HII regions reside is the low N/O envelope. Thus, this suggests that the excursions caused by sudden injections of material are actually upward, toward the region of fewer points. This picture seems consistent with

the lack of evidence for localized oxygen contamination from massive stars in H II regions (Kobulnicky & Skillman 1997). The falloff in points above the N/O envelope is more consistent with injections of nitrogen rather than oxygen. In this case, the nitrogen source might be WR stars or luminous blue variable stars, both of which were considered by Kobulnicky et al. (1997) in their study of nitrogen–enriched H II regions in NGC 5253. They expect also a simultaneous enrichment in helium, and thus H II regions exhibiting high values of N/O should also be checked for evidence of helium enrichment.

8.3. The existing stellar models

For massive stars, there is at present no model producing primary nitrogen unless some ad hoc assumptions are made in order to reproduce the observed N/O ratio at low metallicity (Timmes et al. 1995). In these ad hoc models, some mixing is permitted between the helium– and hydrogen–burning zones. Some primary nitrogen may also be produced in low–metallicity massive stars via some adjusted convective overshoot (Woosley & Weaver 1995). Without any physical explanation, it is difficult to understand why the production of primary nitrogen only occurs at low metallicities. Models of metal free Population III stars (Umeda et al. 2000) produce some primary nitrogen, but in too low quantities to reproduce the observed plateau (see also Heger et al. 2000b).

There is an extensive literature on AGB star models (see for example Forestini & Charbonnel 1997; Boothroyd & Sackmann 1999; Marigo 1998, 2001). Up to the phase of thermal pulses on the AGB branch, the intermediate mass star models predict no primary nitrogen production. Only when the star enters the phase of thermal pulses, some He–burning products may be transported into the H–burning shell, thus producing some primary nitrogen. These models are complex and require a lot of computing time. This is why the AGB models (Renzini & Voli 1981; Marigo 1998) are "synthetic" models, which means that the model parameters follow some analytical relations that have generally been fitted to the observations (this is the case for example for the minimum stellar mass experiencing the third dredge–up). In addition the dependence of this minimum mass on metallicity is based on observation. The same kind of adjustments are made for the occurrence of the hot bottom burning. While this may be useful for some purposes, it cannot be claimed that it represents consistent physics leading to primary nitrogen production. The published stellar yields for intermediate mass stars are generally based on such synthetic models. According to the models of Marigo (2001), the primary nitrogen production depends heavily on the parameters describing the hot bottom burning and the third dredge–up, both processes which are not adequately described in complete stellar models. This means that for intermediate mass stars the primary nitrogen production is not a fully consistent output.

For completness, we also mention here that some explanations of the N/O ratios advocates galactic processes, such as differential outflows of the chemical elements produced by galactic winds (Edmunds 1990). Oxygen is predominantly made in high–mass stars that undergo more violent explosions
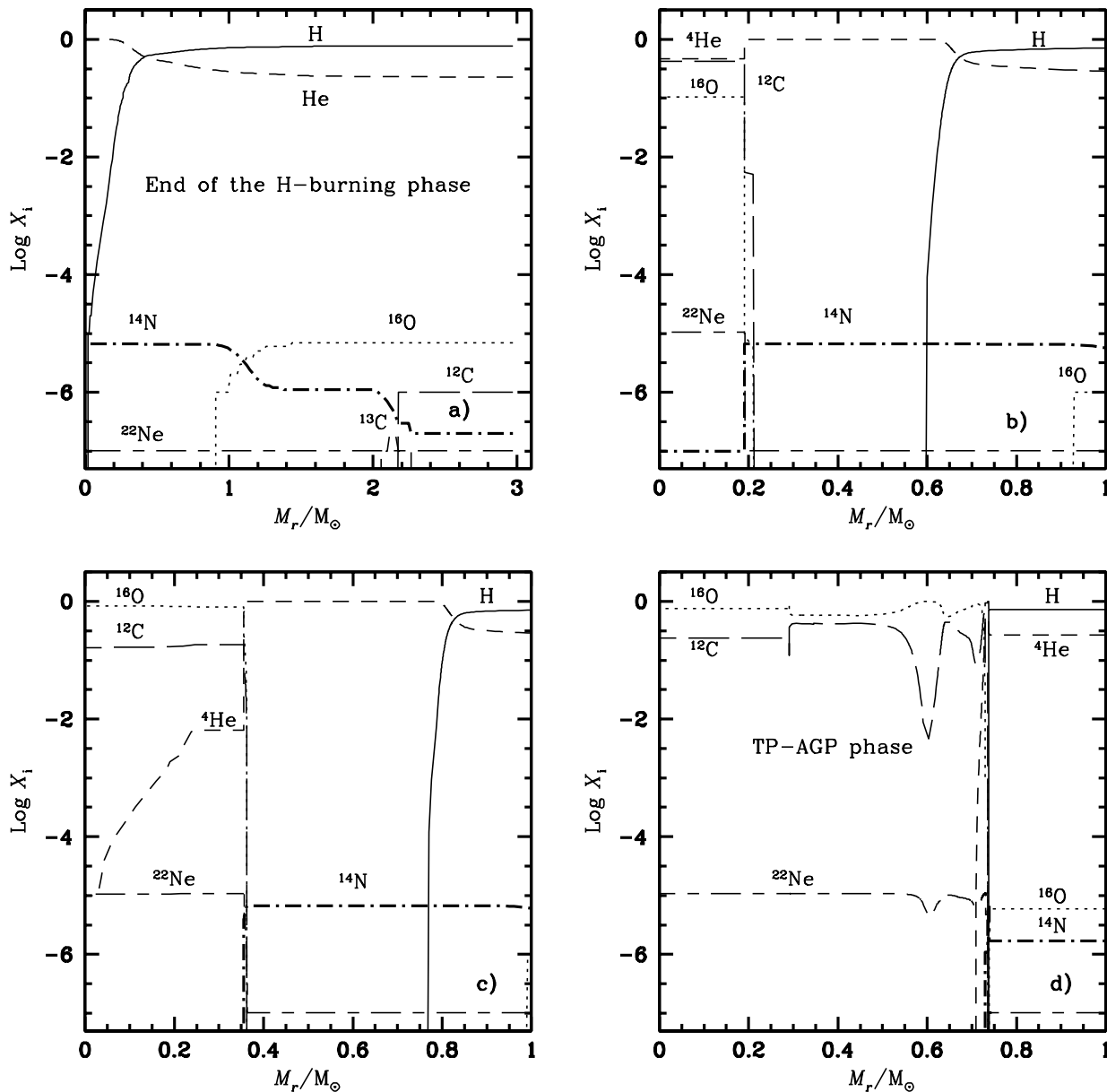
Fig. 13. Variations as a function of the langrangian mass coordinate M_r of the abundances of various elements inside a non–rotating 3 $M_\odot$ model at the metallicity $Z = 10^{-5}$. Panel **a)** shows the chemical structure at the end of the core H–burning phase. Panels **b)** and **c)** at the middle and at the end of the core He–burning phase. The structure after one pulse along the Thermal Pulse–AGB phase is shown on panel **d)**.

than intermediate mass stars, thus is more likely to be removed from the galaxy. This differential outflow results in a decrease in the effective yield for oxygen with a corresponding increase in the N/O ratio. By observing massive spiral galaxies, van Zee et al. (1998) tried to minimize the complicating effects of gas outflow/inflow. They performed nitrogen and oxygen abundance measurements for 185 H II regions spanning a range of radii in 13 spiral galaxies and obtained for the N/O ratios the same behavior as in low–metallicity dwarf galaxies. This result suggests that the observed trend in dwarf galaxies is not due to the outflow of enriched material in a shallow gravitational potential. They conclude that low–metallicity H II regions in all types of galaxies do show evidence of primary nitrogen production.

8.4. The physics of the production of primary nitrogen in low Z rotating models

We need to look with some details the physics which determines the synthesis of primary nitrogen and more generally the particular yields at low Z. Some effects have already been examined by Meynet & Maeder (2002). We organize the discussion in a systematic way:

1) effects of rotation in a 3 $M_\odot$ model at $Z = 10^{-5}$;
2) same problem at $Z = 0.004$ and 0.02;
3) effects of rotation in a 20 $M_\odot$ at $Z = 10^{-5}$, 0.004 and 0.020.

1) Figures 13 and 14 compare the variations of the abundances inside a non–rotating and a rotating 3 $M_\odot$ model with $Z = 10^{-5}$ at various evolutionary stages. At the end of the
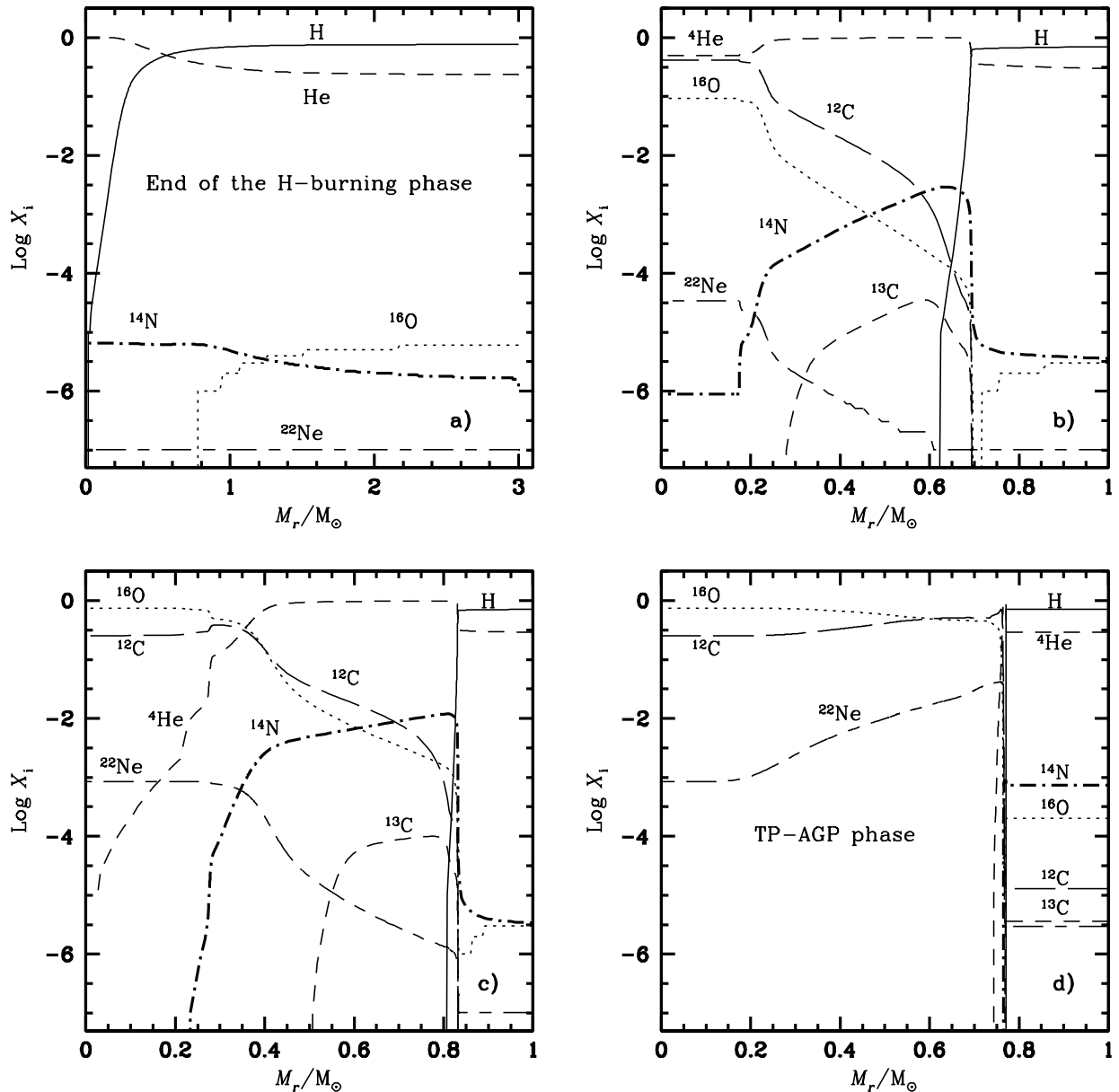
Fig. 14. Same as Fig. 13 for a rotating 3 $M_\odot$ model at the metallicity $Z = 10^{-5}$. The initial velocity on the ZAMS is 300 km s^{-1}, which corresponds to an average surface equatorial velocity during the Main Sequence equal to ~230 km s^{-1}. Panel **a)** shows the chemical structure at the end of the core H–burning phase. Panels **b)** and **c)** at the middle and at the end of the core He–burning phase. The structure after the first five pulses along the Thermal Pulse–AGB phase is shown on panel **d)**.

H–burning phase (panels a), we notice the milder μ–gradient at the very edge of the core, this contributes to make slightly larger He–cores in rotating models. This characteristic is generally larger in larger masses, it also persists and increases in further stages. We notice a significant diffusion of He and N throughout the star in the rotating models. At the middle and at the end of the He–burning phase (panels b and c), the differences in the chemical profiles are striking. In the non–rotating case, there is no new ^{12}C outside the convective core, and therefore there is no primary ^{14}N produced. While in the rotating model, ^{12}C (together with some ^{16}O) is diffusing out the He–burning core and when it reaches the H–burning shell, it is turned by the CNO–cycle into primary ^{14}N, producing a big bump of ^{14}N and a smaller one in ^{13}C. As the H–shell migrates

toward the exterior, the bumps of primary ^{14}N and ^{13}C also progressively extends toward the exterior. The height of these two bumps is growing during the He–burning phase, since diffusion is bringing more and more ^{12}C which is turned to ^{14}N, this explains the growth of the peak in ^{14}N at the outer edge of the intershell region. The abundance of ^{14}N in the rest of the intershell region is also growing with time and this is likely due to the inward diffusion of nitrogen from the peak. Typically, at the end of the He–burning phase, the ^{14}N–abundance in the intershell zone has increased by 3 orders of a magnitude with respect to ^{14}N in the corresponding non–rotating model. At this stage, the integrated quantity of new nitrogen synthesized is $3.22 \times 10^{-3} M_\odot$, while it is only $3.22 \times 10^{-5} M_\odot$ in the non–rotating model.

In further stages, the He–burning shell progresses outwards, letting a degenerate CO core behind it and transforming the ^{14}N into ^{22}Ne (panels d in Figs. 13 and 14). Also in the TP–AGB phase, the content in nitrogen of the outer convective zone increases a lot, due to both the facts that the outer convection zone deepens in mass and that the diffusion at the base of the convective zone continues to proceed. This is saving from destruction a large fraction of the primary nitrogen produced earlier. At the stage shown in Fig. 14 nearly the whole quantity of ^{14}N is in the outer convective envelope. The integrated quantity of primary ^{14}N at this stage is $1.58 \times 10^{-3}\ M_\odot$, i.e. about 50% of what was present in panel c) at the end of the He–burning phase. This fraction of 50% does not change very much during the end of the TP–AGB phase, because the edge of the CO–core and the outer envelope stay very close in lagrangian coordinates. This nitrogen will be ejected by the AGB star either by the superwinds or in the planetary nebula.

In the corresponding non–rotating model (see Fig. 13, panel d), we notice a very similar final structure with a large CO core surrounded by a convective envelope and two thin shells at the basis of it. As only differences, we notice the much smaller ^{14}N and ^{16}O abundances in the envelope. Also, because central degeneracy is higher and thus there is more cooling by neutrinos, the nuclear reaction ^{12}C$(\alpha, \gamma)^{16}$O proceeds farther in the outer core regions than in the inner regions, leading to a kick in ^{12}C and a bump in ^{16}O as observed in panel d of Fig. 13.

The production of ^{13}C in the outer half of the zone between the He–core and the H–burning shell during the He–burning phase is relevant for the nucleosynthesis of "s–process" elements, since ^{13}C is an efficient neutron source. The "s–elements" are produced when ^{13}C is reached by the outer progression of the He–burning shell. Clearly, the formation of "s–elements" is strongly favoured in rotating stars (see also Langer et al. 1999). Amazingly, in the convective envelope, the mass fraction of the CNO elements is about 100 times the initial mass fraction of the heavy elements!

2) It is interesting to compare the above results with those of models of a 3 $M_\odot$ at higher metallicities. Figure 15 shows models with and without rotation for $Z = 0.004$ and 0.020 at the end of the helium burning phase, i.e. corresponding to panel c in Figs. 13 and 14. As usual, the models with zero rotation show flat curves separated by steep transitions due to intermediate convective zones. The models with rotation at $Z = 0.004$ and 0.020 show both the typical internal diffusion profile for ^{12}C and ^{16}O outside the core and noticeably the distributions of ^{14}N are rather similar to that observed for the models at $Z = 10^{-5}$. There is still some quantity of primary nitrogen in the intershell model of the $Z = 0.004$ model, but it is relatively negligible in the $Z = 0.02$ model. The maximum values of ^{14}N in the interior are similar in the three 3 $M_\odot$ models considered, independently of Z.

What are the reasons of this relative constancy? For the models illustrated, the central T are about the same, as normal for He, C, O cores of about the same mass at the middle of the He–burning phase in rotating models. However, the temperatures at the basis of the H–burning shells are different: $\log T = 7.573$ at $Z = 10^{-5}$ and 7.446 at $Z = 0.02$. This is consistent with the fact that the $Z = 10^{-5}$ model is much brighter

($\log L/L_\odot = 2.787$ compared to 2.013 at $Z = 0.02$), because of its much lower opacity. The nuclear energy production (mainly of the H–shell) necessary to supply the stellar luminosity is adjusted, as usual, by the temperature of the shell and not by the content in ^{14}N. The similarity of the distributions of ^{14}N at low metallicity essentially results from the rotational transport of material from the core. We have seen in Sect. 3 that the Ω–distribution during the MS evolutionary phase is different for different Z. However, in later phases the μ–contrast between the dense core and the surrounding layers is about the same and this contrast determines the Ω–gradient and in turn the importance of the diffusion. Thus, the diffusion of ^{12}C outside the core is not very different in models of same mass and rotation, and as a consequence the same is true for ^{14}N.

At $Z = 10^{-5}$ the gradient of ^{14}N between the H–shell and the envelope is much larger than at $Z = 0.02$, because the difference between the peak of ^{14}N in the intershell region and the cosmic abundance in the envelope is also much larger. This has two consequences: firstly, the inward progression of the outer convective zone will bring relatively much more ^{14}N in the envelope; secondly there is also more diffusion of ^{14}N in the envelope at very low Z.

Finally, we also emphasize (cf. Meynet & Maeder 2002) that in the TP–AGB phase the distance between the He– and the H–burning shells is much smaller in lower Z models. This effect will certainly influence considerably the occurrence and properties of the relaxation oscillations. Also, this effect makes the transport of ^{12}C from the He–burning shell to the H–burning shell much shorter, since the timescale for diffusion varies with the square of the distance. In this respect, the smaller intershell region in lower Z models also favours the increase of the abundance of primary nitrogen in the envelope.

In summary, the higher production of primary ^{14}N in very low Z models results mainly from the relatively stronger peak of primary ^{14}N built by rotational mixing in the intershell region during the He–burning phase, a part of which is entering the envelope during its inward migration and another part is brought to the envelope by the diffusion, which is favoured by the smaller intershell region during the TP–AGB phase.

3) Let us examine the 20 $M_\odot$ models at $Z = 10^{-5}$, 0.004 and 0.020. In Fig. 16 for $Z = 10^{-5}$, we see for the rotating model at the middle of the He–burning phase (panel e) the same kind of diffusion profile of ^{12}C and ^{16}O outside the core, as in the corresponding 3 $M_\odot$ model. A similar, although slightly smaller peak of primary ^{14}N is built between the core and the H–shell. Contrarily to smaller masses, where there is no central C–burning, the intershell region remains large. The mainly primary ^{14}N in this region will of course contribute to the yield, as well as that in the outer envelope. The abundance of ^{14}N is increasing in the envelope during He–burning and later phases. Since here, contrarily to the low mass models, there is no inward migration of the envelope, the increase of ^{14}N in the envelope is only due to the diffusion from the ^{14}N gradient in the H–burning shell. As in smaller masses, most of the ^{14}N in the envelope is primary.

When we do a similar study in the 20 $M_\odot$ models at $Z = 0.004$, we notice that there is only a negligible amount of primary ^{14}N produced and the abundance of ^{14}N in the envelope
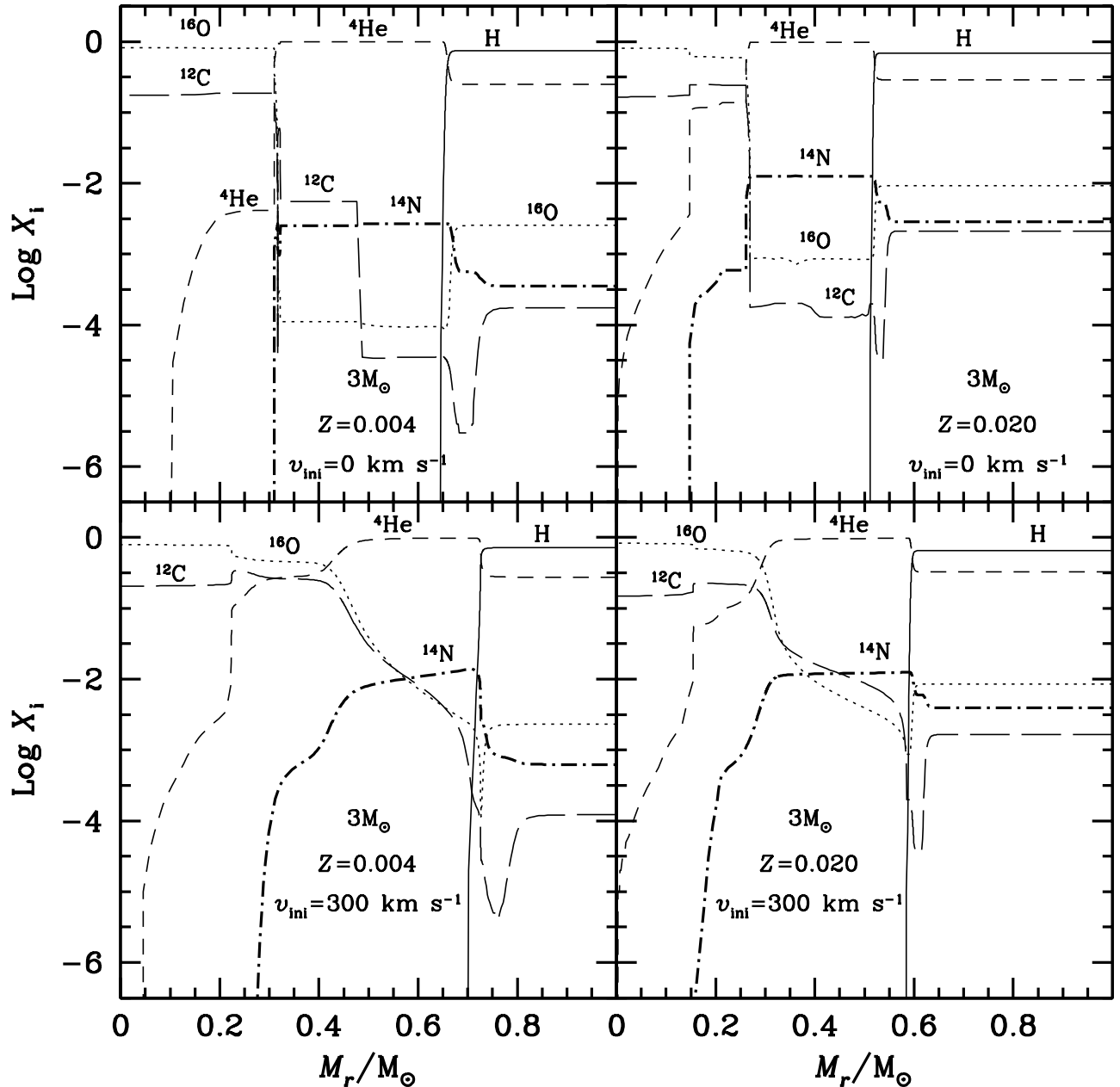
Fig. 15. Variation of the abundances of some elements in the intershell region of 3 $M_\odot$ models at the end of the He–burning phase for the metallicities $Z = 0.004$ and 0.020. The initial velocities v_{ini} are indicated.

of the final models is within a few percents the same in the rotating and non–rotating cases.

In conclusion, we see that there is still some primary nitrogen produced at $Z = 0.004$ in intermediate mass models, as shown by the 3 $M_\odot$ case, but nothing in the high mass stars.

9. The stellar yields

9.1. M_α, M_{CO} and the mass of the remnants, M_{rem}

The computation of the stellar yields, i.e. the quantities of an element newly produced by a star, necessitates, as a first step, the estimate of the masses M_α of the helium cores, M_{CO} of the carbon–oxygen cores, and of the masses M_{rem} of the remnants. These quantities are used for two purposes: 1) To obtain the

oxygen yields using the relation between M_α and the oxygen yields by Arnett (1991). Our models only give an upper limit of the oxygen yields, since they are stopped at the end of the carbon or helium burning phase, i.e. at phases where oxygen has not yet been depleted in the inner regions. 2) To obtain the mass of the remnants using a relation between M_{CO} and M_{rem}. The knowledge of this quantity allows us to calculate the mass of the elements expelled by the supernova. In this work we use the same M_{rem} vs. M_{CO} relation as Maeder (1992). For the intermediate mass stars, we have taken as remnant masses, the mass M_{CO} of the CO core.

Both relations, M_α versus the oxygen yields and M_{CO} versus M_{rem} are deduced from non–rotating models. Ideally one should have used relations obtained from rotating models and
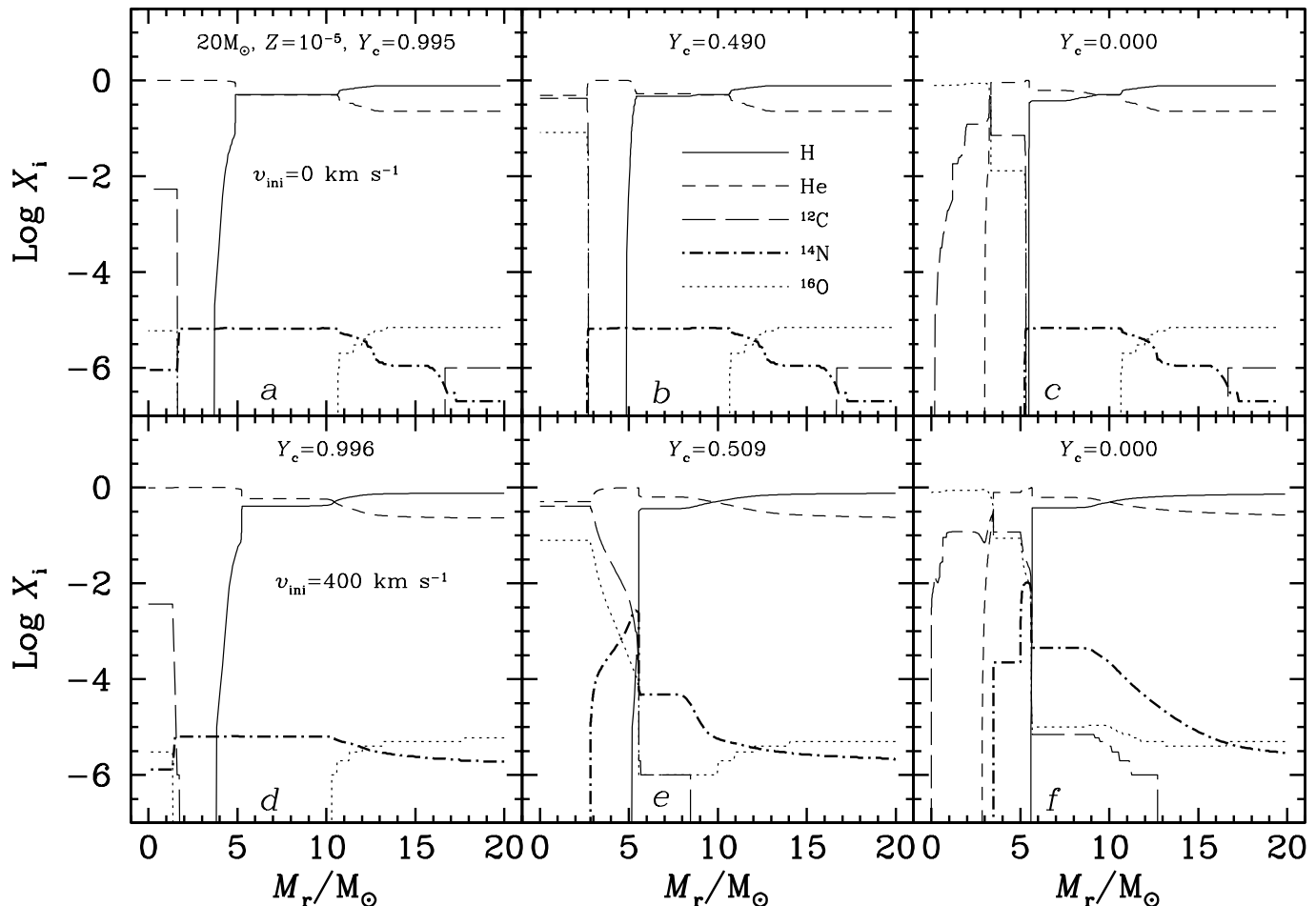
Fig. 16. Variation of the abundances of some elements inside 20 $M_\odot$ models at various stages during the core and shell He–burning phases. The initial metallicity is $Z = 10^{-5}$. The upper panels refer to non–rotating models. Panel **a)** corresponds to the beginning of the core He–burning phase, panel **b)** shows the situation at the middle of the He–burning phase ($Y_c \sim 0.50$) and panel **c)** at the end of the C–burning phase. Panels **d)** to **f)** show the same stages for the corresponding rotating models with $v_{\text{ini}} = 400$ km s^{-1}.

more precisely from rotating models treating the effects of rotation as we did. If such computations would have been available, would the stellar yields be the same? For what concern helium, nitrogen and carbon (although to less extent) the answer is yes. Indeed the parts of the stars which contribute the most to the yields in helium, nitrogen and carbon are in too far out portions of the star for being affected by the M_{CO} versus M_{rem} relation. For the oxygen and heavy element yields, the situation is more complicated. For the moment, we can say that, unless strong and very rapid mixing episodes take place after the end of the carbon burning phase, it is likely that the yields in oxygen and heavy elements obtained here are good estimates of the yields one would have obtained from rotating presupernovae models.

In Table 3, M_α, M_{CO} and M_{rem}, are indicated for different initial mass stars with various metallicities and initial rotation velocities. For initial masses inferior or equal to 7 $M_\odot$, the core masses are estimated after the end of the He–burning phase, during the TP–AGB phase. For higher initial mass models, M_α and M_{CO} are evaluated at the end of the C–burning phase at $Z = 10^{-5}$, except for the 9 $M_\odot$ models with $v_{\text{ini}} = 0$, 200 and 400 km s^{-1} for which the core masses are estimated at the beginning of the C–burning phase. For the models at $Z = 0.004$

(Maeder & Meynet 2001), the core masses are estimated at the end of the He–burning phase. We define M_α as the mass interior to the shell where the mass fraction of helium becomes superior to 0.75. For the rotating 40 and 60 $M_\odot$ models at $Z = 10^{-5}$, the diffusion of helium outside the He–core is so great that the above definition yields an unrealistic high value for the helium core. For these models, we choose to fix the outer border of the He–core at the position where the hydrogen mass fraction goes to zero. Let us note that for the other initial masses this alternative definition of the He–core does not change the results presented in Table 3. The mass of the carbon–oxygen core M_{CO} is the mass interior to the shell where the sum of the mass fractions of ^{12}C and ^{16}O is superior to 0.75.

From Table 3, we note, that rotation in general increases the masses of the helium and CO cores for the massive stars. The reason is that for higher rotation, the intermediate convective zone, associated to the H–burning shell, disappears more quickly. Since the H–burning shell is not replenished in hydrogen, it can more quickly migrate outwards and thus produces the general increase of the He–core mass. However, for the models at $Z = 10^{-5}$ we notice a saturation effect in the increase of M_α for higher rotation and even a decrease for a very

Table 3. Masses of the helium cores, of the carbon–oxygen cores and of the remnants for different initial mass star models with and without rotation at $Z = 10^{-5}$ and 0.004. The masses are in solar mass and the velocities in km s^{-1}.

M	$v_{\rm ini}$	M_α	$M_{\rm CO}$	$M_{\rm rem}$	M_α	$M_{\rm CO}$	$M_{\rm rem}$
		$Z = 10^{-5}$			$Z = 0.004$		
60	0	23.18	18.44	5.68	25.09	20.32	6.26
	300	31.52	26.26	8.03			
40	0	14.05	10.50	3.50	14.61	10.86	3.59
	300	15.38	11.54	3.75	17.87	14.52	4.49
25	0				8.44	5.35	2.25
	300				9.95	7.07	2.69
20	0	5.50	3.35	1.75	6.21	3.57	1.80
	200	7.00	4.66	2.08	7.28	4.64	2.07
	300	6.58	3.92	1.89	7.46	4.80	2.11
	400	5.66	3.45	1.77	7.60	4.94	2.15
15	0	4.15	2.25	1.46	4.45	2.27	1.46
	300	4.99	2.87	1.62	5.01	2.84	1.62
12	0				3.48	1.78	1.34
	300				3.74	1.78	1.34
9	0	2.29	1.12	1.08	2.36	0.87	0.87
	200	2.70	1.40	1.24			
	300	2.53	1.28	1.17	2.85	1.23	1.14
	400	2.51	1.31	1.19			
7	0	1.74	0.90	0.90			
	300	1.07	1.02	1.02			
5	0	1.23	0.75	0.75			
	300	0.88	0.86	0.86			
3	0	0.74	0.73	0.73	0.66	0.46	0.46
	300	0.77	0.76	0.76	0.72	0.66	0.66
2	0	0.62	0.53	0.53			
	300	0.64	0.56	0.56			

Table 4. Stellar yields for helium, carbon, nitrogen, oxygen and the heavy elements from different initial mass stars at $Z = 10^{-5}$ with and without rotation. The initial stellar masses are in solar units. The stellar yields are in solar mass and the velocities in km s^{-1}. The contributions of the stellar winds have been accounted for and are indicated in parenthesis when they exceed one percent of the total yield.

M	$v_{\rm ini}$	$mp_{\rm He4}$	$mp_{\rm C12}$	$mp_{\rm N14}$	$mp_{\rm O16}$	$mp_{\rm Z}$
		$Z = 10^{-5}$				
60	0	1.1e+1	8.4e-1	1.6e-4	1.1e+1	1.3e+1
	300	1.0e+1	6.1e-1	7.0e-4	1.6e+1	1.9e+1
		(0.2e+1)		(0.4e-4)		
40	0	6.9e+0	6.3e-1	1.0e-4	5.0e+0	7.3e+0
	300	8.0e+0	5.8e-1	7.6e-4	5.8e+0	8.2e+0
20	0	3.1e+0	2.2e-1	4.6e-5	5.6e-1	1.7e+0
	200	2.5e+0	2.8e-1	4.2e-5	1.2e+0	2.8e+0
	300	3.3e+0	2.9e-1	3.6e-4	9.9e-1	2.3e+0
	400	3.5e+0	2.9e-1	7.7e-3	6.2e-1	2.0e+0
15	0	2.0e+0	1.2e-1	3.5e-5	1.9e-1	8.6e-1
	300	1.9e+0	1.9e-1	4.1e-4	3.9e-1	1.4e+0
9	0	1.0e+0	1.1e-2	2.2e-5	4.0e-3	5.1e-2
	200	1.1e+0	3.2e-2	7.7e-4	4.0e-3	2.0e-1
	300	1.1e+0	3.6e-2	3.5e-3	4.0e-3	1.6e-1
	400	1.1e+0	4.8e-2	9.2e-3	4.0e-3	2.0e-1
7	0	6.9e-1	1.3e-2	1.6e-5	1.2e-3	1.4e-2
	300	8.0e-1	1.8e-2	4.2e-3	5.6e-3	2.8e-2
5	0	4.1e-1	6.9e-3	1.0e-5	5.6e-4	7.7e-3
	300	4.5e-1	4.5e-3	4.3e-3	1.8e-3	1.1e-2
3	0	9.0e-2	4.7e-4	3.3e-6	8.0e-6	7.0e-4
	300	1.4e-1	2.5e-3	1.6e-3	7.0e-4	5.1e-3
2	0	9.8e-2	1.5e-3	1.7e-6	1.9e-5	1.8e-3
	300	1.2e-1	7.7e-3	6.4e-4	1.1e-3	1.0e-2

high rotation (see the 9 and 20 $M_\odot$ models in Table 3). This behaviour results from the following opposite effect: when rotation increases, the diffusion becomes so efficient that large amounts of hydrogen are brought from the radiative envelope into the H–burning shell. This slows down its outward progression and thus does not produce the growth of the He–core mass in the He–burning phase. As to $M_{\rm CO}$, we see that the variations of $M_{\rm CO}$ with $v_{\rm ini}$ follows those of M_α.

In conclusion, we find that fast rotation in general increases $M_{\rm CO}$ and thus will also increase the yields in α–elements. This is true at very low Z, but not necessarily at solar metallicity, because there fast rotating massive stars will experience high mass loss.

For the intermediate mass stars, the situation is more complicated, since in addition to the effects just mentioned above, the mass of the helium core also results from the inward progression in mass of the outer convective zone during the AGB phase. The deeper this inward extension, the smaller is M_α.

9.2. The stellar yields

In Tables 4 and 5, the stellar yields for helium, carbon, nitrogen, oxygen and for the heavy elements are given for different initial stellar masses with various initial metallicities and rotational velocities. Except for oxygen in massive stars, our models have reached a sufficiently advanced evolutionary stage for the above yields to be directly deduced from our models. The quantity of an element x, newly produced by a star of initial mass m, i.e. the stellar yields in x, is given by

$$mp_x = \int_{M_{\rm rem}}^{M_{\rm fin}} [X_x(m_r) - X_x^0]\,{\rm d}m_r,$$

where $M_{\rm fin}$ is the mass of the star at the end of its evolution, $X_x(m_r)$ is the mass fraction of element x at the langrangian mass coordinate m_r inside the star and X_x^0 is the initial abundance of element x. We consider that the SN ejecta in carbon consist of the C–distribution in the star as it is at the end of the C–burning phase, but we count only the layers which are external to the mass, where carbon is not depleted by the further nuclear burning stages (see Maeder 1992).
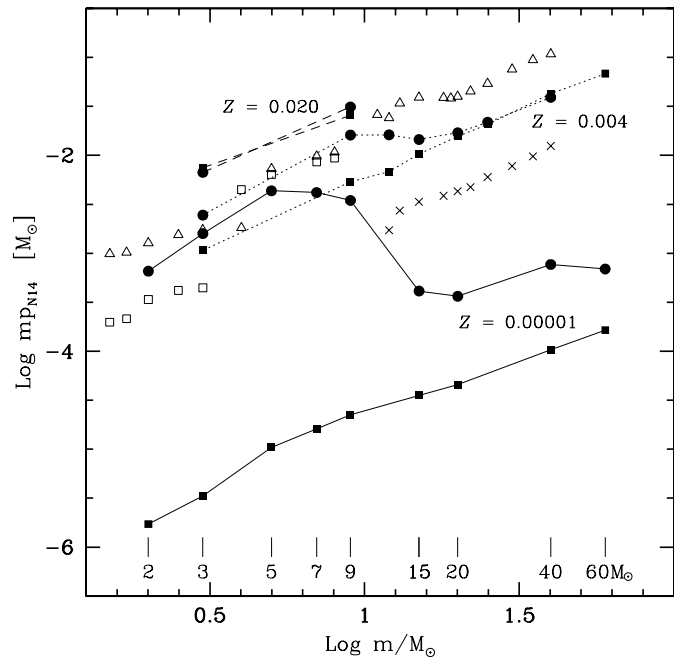
Table 5. Same as Table 4 for the metallicity $Z = 0.004$.

				$Z = 0.004$		
M	v_{ini}	mp_{He4}	mp_{C12}	mp_{N14}	mp_{O16}	mp_Z
60	0	9.3e+0 (2.1e+0)	6.7e-1	6.8e-2 (1.5e-2)	1.2e+1	1.4e+1
40	0	6.3e+0 (0.2e+0)	4.0e-1	4.3e-2 (0.2e-2)	5.3e+0	7.3e+0
	300	5.2e+0 (4.1e+0)	4.9e-1	3.9e-2 (2.6e-2)	7.3e+0	1.0e+1
25	0	3.7e+0	1.1e-1	2.1e-2	1.9e+0	3.1e+0
	300	3.1e+0 (0.1e+0)	2.4e-1	2.2e-2 (0.2e-2)	2.6e+0	4.7e+0
20	0	3.0e+0	8.6e-2	1.6e-2	8.5e-1	1.8e+0
	200	2.7e+0	1.5e-1	1.7e-2	1.3e+0	2.7e+0
	300	2.5e+0	2.1e-1	1.7e-2 (0.1e-2)	1.4e+0	2.9e+0
	400	2.5e+0	2.8e-1	1.7e-2 (0.1e-2)	1.4e+0	3.2e+0
15	0	2.0e+0	3.5e-2	1.0e-2	2.5e-1	8.0e-1
	300	2.0e+0	1.9e-1	1.4e-2	3.9e-1	1.4e+0
12	0	1.4e+0	8.3e-2	6.8e-3	2.7e-2	4.9e-1
	300	1.8e+0	9.3e-2	1.6e-2	7.0e-2	6.0e-1
9	0	1.2e+0	1.4e-2	5.4e-3	4.0e-3	1.6e-2
	300	1.3e+0	4.6e-2	1.6e-2	4.0e-3	1.8e-1
3	0	1.6e-1	8.8e-3	1.1e-3	6.5e-4	1.1e-2
	300	1.3e-1	7.6e-4	2.4e-3	-2.7e-4	3.6e-3

Fig. 17. Variation as a function of the initial mass of the stellar yields in ^{14}N for different metallicities and rotational velocities. The continuous lines refer to the models at $Z = 10^{-5}$ of the present paper, the dotted lines show the yields from the models at $Z = 0.004$ from Maeder & Meynet (2001), the dashed lines present the yields for two solar metallicity models (present work). The filled squares and circles indicate the cases without and with rotation respectively. In this last case $v_{ini} = 300$ km s^{-1}. The crosses are for the models of Woosley and Weaver (1995) at $Z = 0.1 Z_\odot$, the empty squares for the yields from van den Hoek & Groenewegen (1997) at $Z = 0.004$, the empty triangles are for solar metallicity models of van den Hoek & Groenewegen (1997) up to 8 $M_\odot$ and of Woosley and Weaver (1995) above.
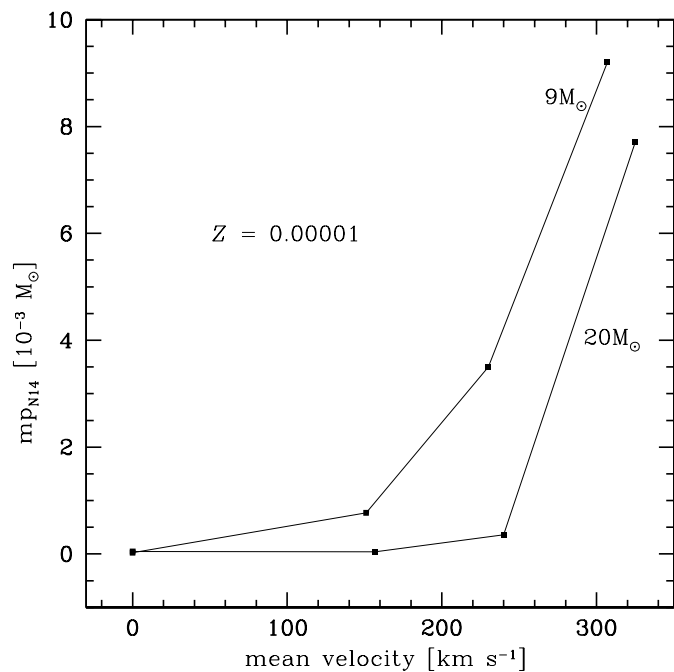
We also accounted for the effects of the stellar winds on the yields as is done in Maeder (1992). In Tables 4 and 5, we have indicated in parenthesis the contribution of the winds when it exceeds one percent of the total stellar yields. For the metallicities considered here, the effects of the winds are small and only modify the yields in helium and nitrogen.

In Fig. 17, the stellar yields in ^{14}N are plotted as a function of the initial mass for different metallicities and rotation velocities. Our non–rotating models (filled squares along the continuous lines) show very small yields at $Z = 10^{-5}$, as expected from a pure secondary origin of ^{14}N. When the effects of rotation are included (filled circles along the continuous lines), the yields for the intermediate mass star models at $Z = 10^{-5}$ become of the same order of magnitude as the yields for the corresponding models at $Z = 0.004$. In this mass range, the yields present thus a very weak metallicity dependence. At solar metallicity, the yields given by the rotating and non–rotating models are identical, this well illustrates the smaller effects of rotation on the nitrogen yields for the higher metallicities.

Figure 18 shows that the ^{14}N stellar yields at $Z = 10^{-5}$ strongly depend on the rotational velocity. Starting from the point at $\bar{v} = 230$ km s^{-1} for the 9 $M_\odot$, an increase of 20% of the mean velocity on the MS, already suffices to double the yield in nitrogen. One notes also the strong increase obtained for the 20 $M_\odot$ when $\bar{v}$ passes from 240 to 325 km s^{-1}. This means

Fig. 18. Variation as a function of the mean velocity during the Main Sequence, $\bar{v}$, of the stellar yields in ^{14}N for a 9 and a 20 $M_\odot$ model at $Z = 10^{-5}$.
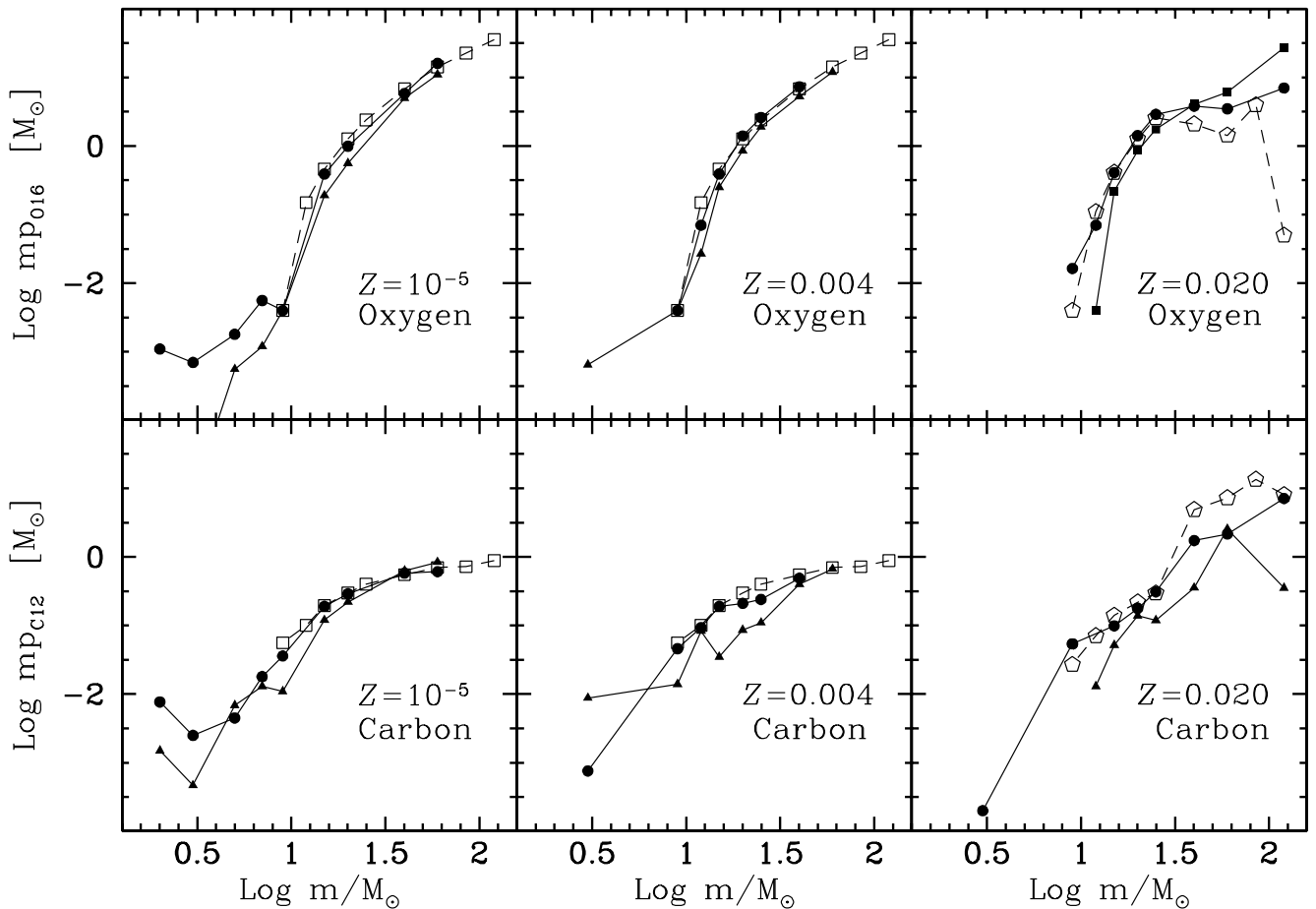
Fig. 19. Variation of the stellar yields in oxygen and carbon as a function of the initial mass, at three different metallicities. The black triangles are for the present non–rotating models, the black circles are for the present rotating models. The empty squares and pentagons are for the stellar yields of Maeder (1992) at the metallicity $Z = 0.001$ and 0.020 respectively.

that if massive stars have sufficiently high initial velocities at low Z, they might also play a role in the production of primary nitrogen (see below).

Figure 19 shows the yields in carbon and oxygen for $Z = 10^{-5}$, 0.004 and 0.020 for models with and without rotation. We notice that the yields of carbon and oxygen (and other heavy elements) are much less affected by rotation than the yields in nitrogen. In general, the yields in carbon, oxygen (and heavy elements) are increased by rotation (cf. Heger 1998), this is a result of the generally bigger value of M_{CO} when rotation is included, as shown above. At solar metallicity, rotation decreases the yield in oxygen because of the higher mass loss, which also produces an increase in the amount of carbon ejected.

How the present stellar yields compare with the yields from other authors? The situation for nitrogen can be seen in Fig. 17, where yields of van den Hoek & Groenewegen (1997, see their Tables 9 and 17) and of Woosley & Weaver (1995, see their models S and P) are plotted. The yields at $Z = 0.004$ of van den Hoek & Groenewegen (1997) for the masses between 5 and 8 $M_\odot$ are higher by about an order of magnitude than the yields of their lower initial mass models. They are nearly at the same level as the yields obtained from the solar metallicity models. This huge enhancement of their ^{14}N stellar yields in

this mass range is a consequence of accounting, in a parameterized way, for the effects of the third dredge–up and of the hot bottom burning, which enable the production of primary nitrogen. The values of the parameters (minimum core mass for the third dredge–up, third dredge–up efficiency, scaling law for mass loss on the AGB, core mass at which the hot bottom burning is assumed to operate) have been chosen in order to reproduce various observational constraints, as e.g. the luminosity function of carbon stars or the abundances observed in planetary nebulae (see van den Hoek & Groenewegen 1997). Interestingly, our rotating models are well in the range of these parameterized yields. Thus rotation, not only naturally leads to the production of primary nitrogen, but also predicts yields in primary nitrogen at a level compatible with those deduced from previous parameterized studies.

One also notes that our yields at $Z = 0.004$ (both from rotating and non–rotating models) are inbetween the yields at $Z = 0.004$ and $Z = 0.020$ of van den Hoek & Groenewegen (1997) and between those of Woosley and Weaver (1995) at $Z \sim 0.002$ and 0.020. This indicates that at higher metallicity, the present yields in nitrogen seem to be in agreement with the yields of other authors. Similar conclusion are reached when comparisons are made between our yields in carbon and

Table 6. Integrated yields in helium, carbon, nitrogen, oxygen and heavy elements (see text).

Z	$12+\log(\frac{O}{H})$	m_d	m_u	v_{ini}	P_{He}	P_C	P_N	P_O	P_Z	$\log \frac{P_C}{P_O}$	$\log \frac{P_N}{P_O}$
10^{-5}	5.74	20	120	0	4.9E-3	3.8E-4	7.4E-8	4.1E-3	5.1E-3	−1.034	−4.743
		8	120	0	7.8E-3	4.9E-4	1.3E-7	4.2E-3	5.8E-3	−0.936	−4.515
		2	120	0	1.1E-2	5.3E-4	2.1E-7	4.2E-3	5.9E-3	−0.900	−4.303
		2	60	0	9.2E-3	4.2E-4	1.8E-7	1.9E-3	3.7E-3	−0.659	−4.013
0.004^a	8.35	20	120	0	4.3E-3	2.5E-4	2.9E-5	4.7E-3	5.6E-3	−1.269	−2.205
		8	120	0	7.3E-3	3.3E-4	4.4E-5	4.9E-3	6.4E-3	−1.175	−2.050
		2	120	0	1.1E-2	4.6E-4	6.5E-5	4.9E-3	6.6E-3	−1.024	−1.878
		2	60	0	9.5E-3	3.6E-4	5.5E-5	2.4E-3	4.0E-3	−0.824	−1.638
0.020^b	8.93	2	120	0	8.9E-3	4.4E-4	3.6E-4	3.3E-3	5.9E-3	−0.881	−0.963
10^{-5}	5.74	20	120	300	4.8E-3	3.3E-4	4.1E-7	6.4E-3	7.7E-3	−1.286	−4.200
		8	120	300	7.7E-3	5.3E-4	3.8E-6	6.8E-3	9.0E-3	−1.106	−3.245
		2	120	300	1.0E-2	6.2E-4	1.1E-4	7.4E-3	9.5E-3	−1.080	−1.833
		2	60	300	1.0E-2	5.4E-4	3.4E-5	2.7E-3	5.0E-3	−0.698	−1.898
0.004^a	8.35	20	120	300	3.7E-3	3.8E-4	2.8E-5	7.0E-3	7.8E-3	−1.265	−2.396
		8	120	300	6.9E-3	5.7E-4	5.8E-5	7.4E-3	9.3E-3	−1.112	−2.109
		2	120	300	1.0E-2	6.2E-4	1.1E-4	7.4E-3	9.5E-3	−1.080	−1.833
		2	60	300	8.8E-3	4.6E-4	9.9E-5	3.4E-3	6.0E-3	−0.871	−1.536
0.020^b	8.93	2	120	300	1.1E-2	1.2E-3	3.9E-4	2.7E-3	6.5E-3	−0.370	−0.844

[a] Models of Maeder & Meynet (2001).
[b] Models of Meynet & Maeder (2000).

oxygen with those of these authors. Our carbon and oxygen yields also compare well with those obained by Maeder (1992) (see Fig. 19).

9.3. Net yields and comparison with the observations

In order to evaluate the impact of these new yields (see Tables 4 and 5) on a galactic scale, we use them in a very simple model of galactic chemical evolution making use of the closed box, instantaneous recycling approximations and supposing a constant star formation rate. We are of course fully aware of the roughness of these approximations, but our intention here is just to estimate the relative effects of rotation on the chemical yields.

In the conditions of this simplified chemical evolution model, the ratio x_i/x_j of the mass fractions of the elements x_i and x_j in the interstellar medium are given by $\frac{x_i}{x_j} = \frac{\widetilde{y_i}}{\widetilde{y_j}}$, where $\widetilde{y_i}$ and $\widetilde{y_j}$ are representative time–independent approximations of the integrated yields of the elements i and j from a stellar generation. The integrated yield of an element x, P_x, is defined as the mass fraction of all stars formed, which is eventually expelled under the form of the newly synthesized element x:

$$P_x = \int_{m_d}^{m_u} m p_x(m)\Phi(m)dm,$$

where $\Phi(m)$ is the Initial Mass Function (IMF). Here we choose a Salpeter IMF, normalized so that

$$\int_{0.1M_\odot}^{120M_\odot} \Phi(m)dm = 1.$$

The masses m_d and m_u limit the mass range of the stars having contributed to the chemical evolution of the interstellar medium at the epoch considered.

In Table 6, the integrated yields are given for various metallicities, initial rotational velocities and values of m_d and m_u. The integrated yields for the solar metallicity have been deduced from the models of Meynet & Maeder (2000). These models have been computed with a different shear diffusion coefficient, and for a different prescription of the mass loss rate than the present models. Therefore they do not belong to the homogeneous set of data constituted by the models at $Z = 10^{-5}$ and 0.004. Despite these differences in the physical ingredients, their properties are well in the lines of the results obtained at lower metallicity. This is the reason why, we have complemented the data of Table 6 with the integrated yields obtained from these models at solar metallicity.
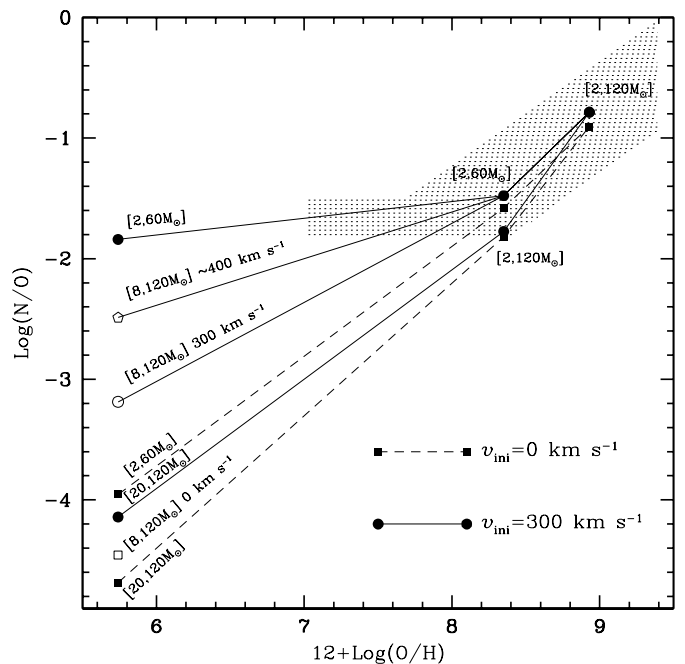
In Figs. 20 and 21, the C/O and N/O ratios, obtained by simply taking the ratios of the corresponding integrated yields, are plotted as a function of O/H. To disentangle the still controversial role of the intermediate mass stars and the effects of rotation, we have taken several values of the upper and lower mass limits. We have considered at $Z = 10^{-5}$ the 20 to 120 $M_\odot$
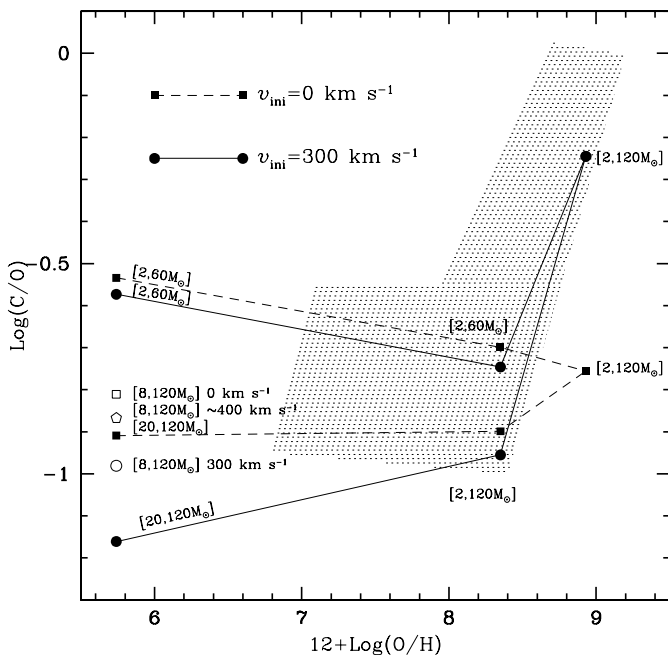
Fig. 20. Simplified model for the galactic evolution of the C/O ratio as a function of the O/H ratio (in number). The dashed and continuous lines show the results deduced from the non–rotating and the rotating models respectively (see text). The range of the initial masses used for computing the integrated yields are indicated. The empty symbols show the results when only stars more massive than 8 $M_\odot$ are considered. The initial velocity is indicated. The shaded area shows the region where most of the observations of extragalactic HII regions and stars are located (see e.g. Gustafsson et al 1999; Henry et al. 2000).

Fig. 21. Same as Fig. 20 for the N/O ratio.

interval, that of 8 to 120 $M_\odot$ and that of 2 to 60 $M_\odot$. In each case, the models without rotation and with an initial rotation of 300 km s^{-1} (i.e. an average of 230 km s^{-1} during the MS phase) have been considered. In addition, for the case of 8 to 120 $M_\odot$ an initial rotation of 400 km s^{-1} has also been considered. At $Z = 10^{-5}$, we notice that rotation only slightly decreases the C/O ratio, the effect is a bit larger when only massive stars are considered. This behaviour is due to the growth of M_{CO} with rotation, which favours the production of O more than that of C. However, we emphasize that the effect of the mass interval is more important than rotation. When the intermediate mass stars are included, the C/O ratio is as expected much larger. In summary, at low Z, the diagram C/O vs. O/H is particularly sensitive to the mass interval.

Between $Z = 0.004$ and 0.02, the main effect influencing the C/O ratio is no longer the value of M_{CO} as above, but the effects of stellar winds and their enhancement by rotation. Rotation favours a large C/O ratio, because rotating models enter at an earlier stage into the Wolf–Rayet phase than their non–rotating counterparts. As a consequence, in rotating models at $Z = 0.02$, great quantities of carbon are ejected by the massive stars through their stellar winds, when they become a Wolf–Rayet star of the WC type. This is quite in agreement with the results by Maeder (1992) who showed that when the mass loss rates are high, most of the carbon is produced and ejected by massive stars through their stellar winds. In non–rotating models, the new mass loss rates used here are much lower than those

used in 1992 because now the mass loss rates account for the clumping effects in the Wolf-Rayet stellar winds.

The diagram N/O vs. O/H (Fig. 21) has a different sensitivity to the mass interval and rotation. At very low Z, we notice a very high sensitivity to rotation when the lowest mass limit is at 2 or 8 $M_\odot$; this is due to the production of primary nitrogen. The increase in the N/O ratio may reach more than 2 orders of a magnitude. Contrarily to the previous diagram, the N/O ratio is not sensitive at all to the mass interval for models without rotation. Thus, *the combination of the diagrams C/O vs O/H, more sensitive to the mass interval, and of the diagram N/O vs. O/H, more sensitive to rotation, may be particularly powerful to disentangle the two effects of rotation and mass interval, and to precise the properties of the star populations responsible for the early chemical evolution of galaxies.*

At the present stage, when we compare our results to the observations we may derive the following tentative conclusions, which could change if the data further improve. The C/O vs O/H diagram does not seem favorable to enrichments by only very massive stars in the range 20 to 120 $M_\odot$; contributions from stars down to 8 or 2 $M_\odot$ may be needed, depending on the exact slope observed at low Z in Fig. 20. As to the N/O vs. O/H diagram, no model without rotation is able to account for the observed plateau, moreover contributions from only stars above 20 $M_\odot$ seem difficult. The observed plateau at log N/O = −1.7 strongly supports rotating models including the large contribution from intermediate mass stars down to, either 2 $M_\odot$ if these stars have the same average rotation as in Pop. I stars, or down to only 8 $M_\odot$ if the rotations are faster as suggested by Maeder et al. (1999). In this respect, it would be sufficient that the average rotational velocities during the MS phase are larger by about 80 km s^{-1}.

We must temper these conclusions by the following remark (cf. also Meynet & Maeder 2002), related to a current

problem in the chemical evolution of galaxies. Nitrogen is ejected mainly by AGB stars with ejection velocities of a few 100 km s^{-1}, while oxygen is ejected by supernovae at much higher velocities of 10^4 km s^{-1} or more. Thus, a fraction of the oxygen produced may escape from the parent galaxy, leading to a higher N/O ratio than in the simple estimate made here.

10. Conclusions

We have investigated in some detail the physics of very low Z models with $Z = 10^{-5}$. Even if we have little chance of observing such star populations, these models are most relevant for the early chemical evolution of galaxies. The models enable us to calculate the yields in CNO, He and heavy elements necessary to study the early evolution of galaxies. The diagrams showing log N/O vs. log O/H and log C/O vs. O/H are particularly powerful to infer properties of the early star generation in galaxies.

This work shows the large differences brought by the present models with rotation. In future we shall calculate the detailed yields of the various heavy elements.

References

Arnett, D. W. 1991, in Frontiers in Stellar Evolution, ed. D. A. Lambert, ASP Conf. Ser., 20, 389

Arnett, D. W. 1996, Supernovae and Nucleosynthesis (Princeton Univ. Press), 188

Angulo, C., Arnould, M., Rayet, M., et al. 1999, Nucl. Phys. A, 656, 3

Barbuy, B. 1983, A&A, 123, 1

Boothroyd, A. I., & Sackmann, I. J. 1999, ApJ, 510, 232

Carbon, D .F., Barbuy, B., Kraft, R. P., Friel, E. D., & Suntzeff, N. B. 1987, PASP, 99, 335

Clayton, D. 1983, Principles of stellar evolution and nucleosynthesis (Chicago, University of Chicago Press)

Denissenkov, P. A., Ivanova, N. S., & Weiss, A. 1999, A&A, 341, 181

Edmunds, M. G. 1990, Nature, 348, 395

Edmunds, M. G., & Pagel, B. E. J. 1978, MNRAS, 185, 77

Fagotto, F., Bressan, A., Bertelli, G., & Chiosi, C. 1994, A&AS, 104, 365

Ferguson, A. M. N., Gallagher, J. S., & Wyse, R. F. G. 1998, AJ, 116, 673

Forestini, M., & Charbonnel, C. 1997, A&AS, 123, 241

Garnett, D. R. 1990, ApJ, 363, 142

Garnett, D. R., Shields, G. A., Skillman, E. D., Sagan, S. P., & Dufour, R. J. 1997, ApJ, 489, 63

Girardi, L., Bressan, A., Chiosi, C., Bertelli, G., & Nasi, E. 1996, A&AS, 117, 113

Gustafsson, B., Karlsson, T., Olsson, E., Edvardsson, B., & Ryde, N. 1999, A&A, 342, 426

Heger, A. 1998, Ph.D., Max–Planck–Institut für Astrophysik, München

Heger, A., & Langer, N. 2000, ApJ, 544, 1016

Heger, A., Langer, N., & Woosley, S. E. 2000, ApJ, 528, 368

Heger, A., Woosley, S. E., & Waters, R. 2000, The First Stars, the MPA/ESO Workshop, ed. A. Weiss, et al., 121

Henry, R. B. C., & Worthey, G. 1999, PASP, 111, 919

Henry, R. B. C., Edmunds, M. G., & Köppen, J. 2000, ApJ, 541, 660

van den Hoek, L. B., & Groenewegen, M. A. T. 1997, A&AS, 123, 305

Iglesias, C. A., & Rogers, F. J. 1996, ApJ, 231, 384

Israelian, G., Rebolo, R., Garcia Lopez, R. J., et al. 2001, ApJ, 551, 833

Izotov, Y. I., & Thuan, T. X. 1999, ApJ, 511, 639

Izotov, Y. I., & Thuan, T. X. 2000, New Astron. Rev., 44, 329

Izotov, Y., Schaerer, D., & Charbonnel, C. 2001, ApJ, 549, 871

Kobulnicky, H. A., & Skillman, E. D. 1996, ApJ, 471, 211

Kobulnicky, H. A., & Skillman, E. D. 1997, ApJ, 489, 636

Kobulnicky, H. A., Skillman, E. D., Roy, J. R., Walsh, J. R., & Rosa, M. R. 1997, ApJ, 477, 679

Kudritzki, R. P., & Puls, J. 2000, Ann. Rev. Astron. Astrophys., 38, 613

Kunth, D., Matteucci, F., & Marconi, G. 1995, A&A, 297, 634

Langer, N. 1998, A&A, 329, 551

Langer, N., Heger, A., Wellstein, S., & Herwig, F. 1999, A&A, 346, L37

Lu, L., Sargent, W. L. W., Savage, B. D., Wakker, B. P., et al. 1998, AJ, 115, 162

Maeder, A. 1992, A&A, 264, 105

Maeder, A. 1997, A&A, 321, 134 (Paper II)

Maeder, A., & Meynet, G. 2000, A&A, 361, 159 (paper VI)

Maeder, A., & Meynet, G. 2001, A&A, 373, 555 (Paper VII)

Maeder, A., & Peytremann, E. 1970, A&A, 7, 120

Maeder, A., & Zahn, J. P. 1998, A&A, 334, 1000 (Paper III)

Maeder, A., Grebel, E., & Mermilliod, J. C. 1999, A&A, 346, 459

Marigo, P. 1998, A&A, 340, 463

Marigo, P. 2001, A&A, 370, 194

Marigo, P., Girardi, L., Chiosi, C., & Wood, P. R. 2001, A&A, 371, 152

Matteucci, F. 1986, MNRAS, 221, 911

Melendez, J., Barbuy, B., & Spite, F. 2001, ApJ, 556, 858

Meynet, G., & Maeder, A. 1997, A&A, 321, 465 (Paper I)

Meynet, G., & Maeder, A. 2000, A&A, 361, 101 (Paper V)

Meynet, G., & Maeder, A. 2002, A&A, 381, L25

Pettini, M., Lipman, K., & Hunstead, R. W. 1995, ApJ, 451, 100

Renzini, A., & Voli, M. 1981, A&A, 94, 175

Rudolph, A. I., Simpson, J. P., Haas, M. R., Erickson, E. F., & Fich, M. 1997, ApJ, 489, 94

Skillman, E. D., Bomans, D. J., & Kobulnicky, H. A. 1997, ApJ, 474, 205

Talbot, R. J., & Arnett, W. D. 1974, ApJ, 190, 605

Talon, S., & Zahn, J. P. 1997, A&A, 317, 749

Talon, S., Zahn, J. P., Maeder, A., & Meynet, G. 1997, A&A, 322, 209

Thuan, T. X., Izotov, Y. I., & Lipovetsky, V. A. 1995, ApJ, 445, 108

Timmes, F. X., Woosley, S. E., & Weaver, T. A. 1995, ApJS, 98, 617

Tomkin, J., & Lambert, D. L. 1984, ApJ, 279, 220

Umeda, H., Nomoto, K., & Nakamura, T. 2000, The First Stars, the MPA/ESO Workshop, ed. A. Weiss, et al., 137

Vilchez, J. M., & Esteban, C. 1996, MNRAS, 280, 720

Woosley, S. E., & Weaver, T. A. 1995, ApJS, 101, 181

van Zee, L., Salzer, J. J., & Haynes, M. P. 1998, ApJ, 497, L1